Perspective

Opportunities at the Intersection of 3D Printed Polymers and Pyrolysis for the Microfabrication of Carbon-Based Energy Materials

Published as part of JACS Au special issue "Polymers for the Clean Energy Transition".

Philip R. Onffroy,[¶] Samuel Chiovoloni,[¶] Han Lin Kuo, Max A. Saccone,* Jennifer Q. Lu,* and Joseph M. DeSimone*

Cite This: *JACS Au* 2024, 4, 3706−3726

Read Online

ACCESS | 📊 Metrics & More | 📑 Article Recommendations | 🆘 Supporting Information

ABSTRACT: In an era marked by a growing demand for sustainable and high-performance materials, the convergence of additive manufacturing (AM), also known as 3D printing, and the thermal treatment, or pyrolysis, of polymers to form high surface area hierarchically structured carbon materials stands poised to catalyze transformative advancements across a spectrum of electrification and energy storage applications. Designing 3D printed polymers using low-cost resins specifically for conversion to high performance carbon structures via post-printing thermal treatments overcomes the challenges of 3D printing pure carbon directly due to the inability of pure carbon to be polymerized, melted, or sintered under ambient conditions. In this perspective, we outline the current state of AM methods that have been used in combination with pyrolysis to generate 3D carbon structures and highlight promising systems to explore further. As part of this endeavor, we discuss the effects of 3D printed polymer chemistry composition, additives, and pyrolysis conditions on resulting 3D pyrolytic carbon properties. Furthermore, we demonstrate the viability of combining continuous liquid interface production (CLIP) vat photopolymerization with pyrolysis as a promising avenue for producing 3D pyrolytic carbon lattice structures with 15 μm feature resolution, paving way for 3D carbon-based sustainable energy applications.

KEYWORDS: *3D printing, pyrolysis, energy storage, polymers, 3D carbon*
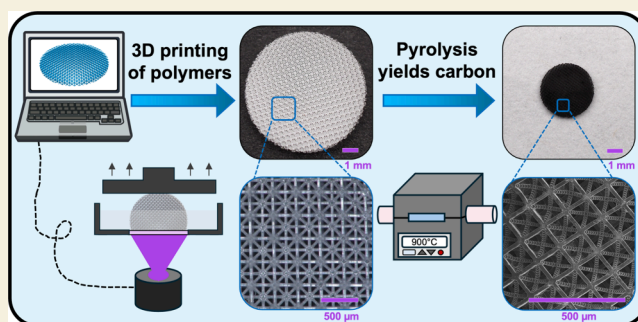
1. INTRODUCTION

In recent years, additive manufacturing (AM), or 3D printing, has enabled the development of highly replicable polymer structures with features on the scale of single microns.[1−3] AM is a software-controlled process for producing objects layer-by-layer that enables advanced fabrication of highly tunable and complex geometries, for example beam-based lattices, circumventing the constraints of traditional subtractive or molding methods.[4,5] Carbon is a low-cost element with high abundance in nature. While 3D printing enables a high degree of flexibility in the geometry of printed parts, 3D printing cannot produce pure carbon structures under ambient conditions directly without further processing steps.[6] 3D carbon structures offering high electrical conductivity and chemical stability have demonstrated potential to be used as 3D electrodes.[1,7]

Conducting a high temperature thermal treatment primarily under an inert atmosphere (argon or nitrogen gas) is called pyrolysis, and this process is often conducted on polymeric materials to initiate carbonization of polymer chains into fully carbonaceous structures.[8] Carbon-based materials can be classified into three primary groups: amorphous carbon; semicrystalline carbon, also known as glassy carbon; and highly crystalline carbon, also known as graphitic carbon. Typically, the goal of pyrolysis is to eliminate noncarbon elements in a polymer (e.g., oxygen and hydrogen) and induce graphitization, the formation of highly stable sheets of trigonal planar sp^2 hybridized carbon.[6,9] The high electrical conductivity of graphitic carbon produced in this manner arises due to the presence of delocalized pi (π) electrons, which are free to move throughout the material.

The formation of structurally stable graphitic pyrolytic carbon requires a high surface area-to-volume ratio (S_V) to enable volatile byproducts created during carbonization to escape from within the depths of thicker features. Mechanical deformations and defects can result from built-in stress caused
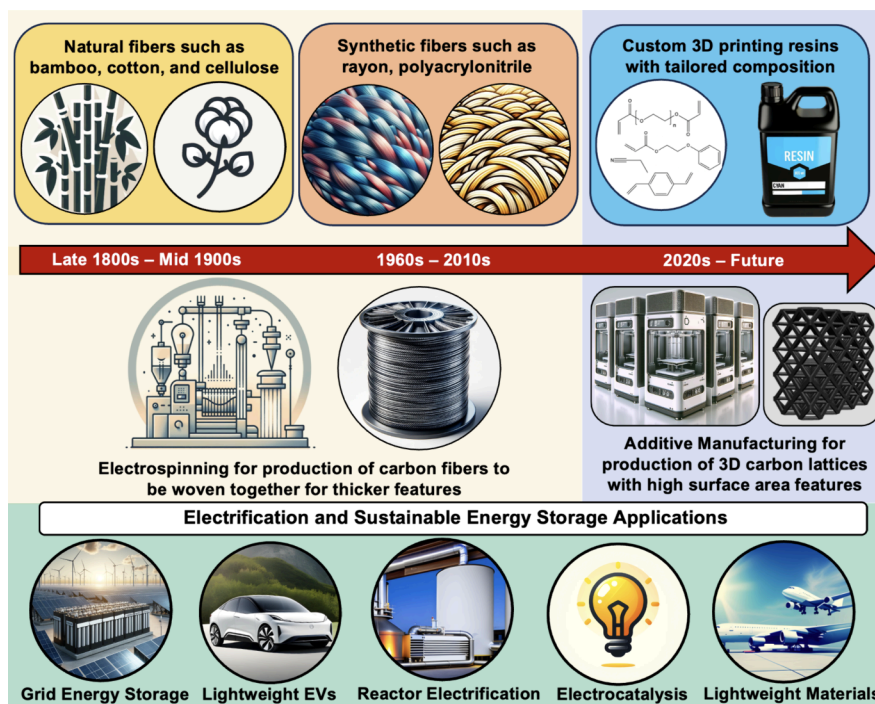
Figure 1. Historical context for pyrolytic carbon feedstock (top row) and production (middle) leading up to several modern applications (bottom).

by trapped volatiles during the pyrolysis process. Heat transfer concerns during pyrolysis can also arise with thicker solid objects leading to heterogeneities.[8,10] Polymer structures with thinner features and high void fractions better facilitate volatiles escaping during heating without deformation due to shorter diffusion pathlengths.[10] AM can generate high surface area structures such as beam-based lattices that achieve the desired high S_V characteristic needed for chemical conversion via pyrolysis.[11] Transforming 3D printed polymer lattices into carbon via subsequent pyrolysis therefore is an attractive approach for converting 3D printed structures into pure carbon. This technique has generated structures with high S_V suitable for applications in structural materials,[12,13] heterogeneous electrocatalysis,[14,15] biosensors[16,17] and renewable energy storage.[18-20] Thus, the convergence of AM with pyrolysis is poised to contribute to achieving a sustainable future.[1]

Herein, we will review the current state of research into pyrolysis of 3D printed polymers to pyrolytic carbon structures. While there exists substantial interest in the generation of polymer-derived structural and functional ceramics (e.g., semiconductors, ceramic batteries) via 3D printing techniques such as precursor infiltration and pyrolysis (PIP), this review will focus on 3D carbon-based materials produced via carbonization of polymers, so the reader is directed to other reviews that focus on ceramics.[21-23] Previous reviews have also discussed the production of carbonaceous materials with 3D printing via carbon-filled composites, inclusion of graphene oxide in resins, and pyrolysis of 3D printed carbon precursors[6,24-26] and 3D printed aerogels.[1] Here, we add to this body of literature by focusing on the polymer resin compositions used for generating 3D carbon material, the geometry and feature size limits of 3D printed structures during pyrolysis, and the pyrolysis heat treatment conditions used to convert the polymeric structures to conductive carbon. To accomplish this, we begin with an

overview of the 3D printing methods used with pyrolysis to date to generate carbon-based materials (Section 2). We then survey the current literature to elucidate the effects of polymer molecular composition (Section 3) and pyrolysis conditions (Section 4) on resultant carbon materials for use in several energy, catalysis, and biomaterial applications (Section 5). Finally, in Section 6, we introduce the use of continuous liquid interface production vat photopolymerization, which has already been scaled to an industry level, in conjunction with pyrolysis to generate high resolution, conductive carbon lattices, paving way for next generation carbon lattice structures for advancement of global sustainable energy and electrification.

2. 3D PRINTING METHODS USED WITH CONVENTIONAL PYROLYSIS THERMAL TREATMENTS

Pyrolysis of polymeric materials has origins going back to the charcoal used in prehistoric times.[27] In the modern materials industry, pyrolysis has been used for over a century to produce high strength, conductive carbon structures, most prominently in the carbon fiber industry.[28,29] In the late 1800s through mid 1900s, the polymers used for carbon fiber production were initially sourced from natural feedstocks, such as bamboo shafts, cotton threads, and cellulose. In the 1960s, the industry transitioned from natural materials to synthetic fiber feedstocks, such as rayon and polyacrylonitrile, which are still used today.[30] Carbon fibers, with diameters of 5−10 μm, have been the state-of-the-art material in the pyrolysis field and are woven together for use in applications ranging from the electrical components in light bulbs to the heat-resistant fan blades in jet engines.[31] However, pyrolysis of nonfibrous thicker 3D structures has been a relatively unexplored area due to the diffusion issues faced by volatile components escaping polymeric structures during pyrolysis. As illustrated in Figure 1, scalable AM in combination with pyrolysis has recently been

utilized to overcome this challenge and generate thick (≥cm scale) pyrolytic carbon objects with micro- or nanoscale features that enable high S_V desirable in sustainable applications in the ongoing energy industry shift toward electrification and reliance on batteries for renewable energy storage.[32]

The process of AM generates 3D objects using digital graphic data and is principally practiced using either extrusion techniques, powder sintering techniques, or light-based photopolymerization techniques.[33] Most approaches for pyrolysis of 3D printed structures to date are plagued by low carbon yields, high degrees of volume shrinkage, and structural warping during the polymer-to-carbon conversion.[13,19,34−36] While some researchers have accommodated these challenges by designing the as-printed parts to account for large shrinkages,[32,37] others have sought to utilize this shrinkage to their advantage.[12,38] Strategies to mitigate shrinkage include incorporating carbon-based resin additives to increase char yields,[39,40] conducting preoxidation of the printed parts to reduce internal stresses developed during printing,[19,34] and designing custom resin formulations.[19,34,35] Interest in the combination of 3D printing and pyrolysis has increased rapidly over the past several years, evidenced by the increase in number of Google Scholar citations mentioning 3D printing, pyrolysis, and pyrolytic carbon (Figure 2).
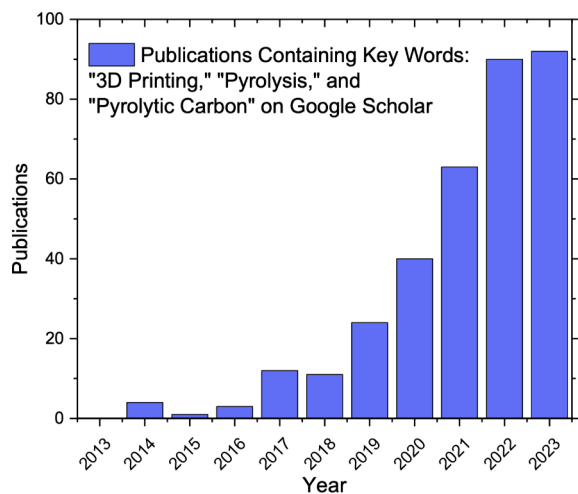

Figure 2. Histogram displaying the recent increase in prevalence of 3D printing and pyrolysis literature in Google Scholar from 2013 to 2023.

There are many methodologies that can accomplish 3D printing. The family of extrusion-based 3D printing techniques, such as direct ink writing (DIW)[1,18,41,42] and fused filament fabrication (FFF),[43,44] is widely employed for layer-by-layer printing to create 3D periodic lattices. For example, DIW using inks containing a high percentage of carbon nanostructures (e.g., graphene) has been used with pyrolysis to produce thick conductive carbon aerogels for energy storage.[1,18,42,45] Ink formulations for DIW are generally constrained to thixotropic and shear-thinning materials to prevent deformation of printed structures,[46] whereas ideal DIW inks have high viscosity and demonstrate solid-like behavior at zero shear. Further, such direct-write fabrication processes are challenging to scale due to their limited throughput at the necessary high resolution needed for achieving the S_V electrode manufacturing goals later described in Section 5, outside of certain material systems such

as polyelectrolytes that are not applicable in pyrolytic carbon production.[47] Another AM method of note for carbon production is aerosol-jet microscale printing, which uses an ultrasonic actuator to atomize carbon precursors in an aerosol stream and deposit graphene ink via a nozzle with resolution down to 10 μm, without the need for a pyrolysis step.[48]

Alternatively, vat photopolymerization (VP)[37] 3D printing is a category of techniques that employs the selective curing of photoresins with light. VP approaches are split into three subclassifications: (1) raster-based methods including scanning stereolithography (SLA) and direct laser writing via two-photon polymerization (DLW-2PP),[49] (2) volumetric additive manufacturing including computed axial lithography (CAL)[50] and xolography,[51] and (3) pattern projection-based methods including digital light processing (DLP),[32] projection micro stereolithography (PμSL),[52] and continuous liquid interface production (CLIP).[53] VP currently is a scalable technology for producing complex lattice structures that cannot be produced via traditional molding methods due to the high speed and resolution capabilities afforded by using light-based radical polymerization.[54] The DLP and CLIP techniques in particular offer excellent combinations of higher throughput, with linear speeds up to 17 mm/min, precision, and scalability, as the entire liquid vat surface is exposed to UV light patterns controlled via a digital micromirror device.[54−56] For more information on printing rates and scalability of the aforementioned AM methods, the reader is directed to recent studies that focus on 3D printing speed and comparisons of photopolymerization approaches.[54,55,57]

The prevalence of which AM methods have been used in combination with pyrolysis in recent literature is overviewed in Table 1. This summary demonstrates that there is a significant representation from both the extrusion (DIW, FFF) and the photopolymerization (SLA, DLW-2PP, DLP, PμSL, CLIP) methods. The reported SLA category serves as a catch-all classification for laser-based photopolymerization methods that do not fit into DLW-2PP or other VP categories. The extrusion techniques commonly generate structures with features on the millimeter scale, with one instance of DIW achieving 100 μm features,[45] while the photopolymerization techniques demonstrate feature sizes ranging from as low as 100 nm for DLW-2PP[58] to 2 μm for SLA,[17] 28 μm for DLP,[32] and 10 μm for PμSL.[52] The pyrolysis furnace upper-end temperature for 3D printed structures ranges from 430 to 1300 °C in these studies, with the greatest abundance of studies using between 900 and 1000 °C as their final temperature.

3D printing techniques such as DIW and FFF are typically used to generate samples with features on the millimeter scale. Several of these extrusion-based 3D printing studies utilize biomass, such as cellulose-based compounds, due to evidence of these polysaccharide biomass materials generating high yield pyrolytic carbon outputs[44,60,78] However, structures produced using biomass components alone appear relatively granulated and inhomogeneous, and it has been reported that 3D printed biomass carbon precursors do not demonstrate degrees of graphitization as high as their synthetic polymer counterparts.[79] To bypass this challenge, various additives have been mixed into biomass-containing melt extrusion 3D printing materials for enhanced electrical properties and stability, for example metal organic frameworks (MOFs)[60] and graphene oxide (GO) nanoparticles.[45]

Alternatively, stereolithography 3D printing methods have been used more prominently in conjunction with pyrolysis, due

Table 1. Summary of Current Additive Manufacturing (AM) Methods Used in Combination with Pyrolysis for Generation of Pyrolytic Carbon

AM Method	Pyrolyzed Material Feature Size	Resin	Application	Furnace Conditions	Reference
Direct ink writing (DIW)	mm scale	Pluronic F127, activated carbon	Gas separation, adsorption, and desorption of CO2	900 °C final, 10 °C/min ramp	59
	100 μm	Hydroxypropyl methylcellulose and GO	Electrodes for Energy Storage	1050 °C final, 2 °C/min ramp	45
	mm scale	Cellulose and ZIF-8 MOF	Capacitors and Electrodes	1000 °C, 5 °C/min	60
Fused filament fabrication (FFF)	500 μm	Cellulose, lignosulfonate	Electrodes for Energy Storage	1200 °C final, various holds, 0.2 °C/m ramp	44
	mm scale	Polyacrylonitrile, solketal acrylate	High Capacitance Supercapacitors	1000 °C final, 200 and 260 °C air hold, 0.5 °C/min ramp	43
Direct laser writing via two-photon polymerization (DLW-2PP)	170 nm	Organic–inorganic SZ2080	Fiber optics	600 °C final	61
	170 nm	Custom acrylates: PEGDA, PETA, ZIF-8 MOF	Semiconductors	550 °C final, 20 °C/s ramp	62
	1 μm	IP-Dip (Nanoscribe GmbH)	High Strength Structural Applications	1000 °C final, 450 °C, 500 °C, 550 °C holds, 20 °C/s ramp	36
	250 nm	IP-Dip (Nanoscribe GmbH)	Electroforming, Template-assisted electrodeposition	500 °C final, 5 °C/min ramp	63
	100 nm	Custom acrylates: PRM30 and PETA	High Strength Structural Applications	1100 °C final, various holds, 3 °C/min ramp	64
	2–10 μm	IP-Dip (Nanoscribe GmbH)	Mechanics, Optics, Medical Detection	500 °C final	65
	100 μm	IP-S (Nanoscribe GmbH)	Neurotransmitter Detection	900 °C final	58
	135 μm	IP-Q (Nanoscribe GmbH)	Batteries, material engineering, and catalysts	Various temperatures up to 600 °C, 10 °C/min ramp	49
	200 μm	IP-Dip (Nanoscribe GmbH)	High Strength Structural Applications	900 °C final, 250 and 350 °C hold, 3 °C/min ramp	12
Stereolithography apparatus (SLA)	316 μm	SU-8, High Temperature (HT) V1	Electrodes for Energy Storage	900 °C final	66
	10 μm	SU-8	Batteries, fuel cells, sensors, filters	1300 °C, 1150 °C, 900 °C, 600 °C finals	67
	2 μm	SU-8	Microelectrode chips for biochemical sensing	900 °C final, 200 °C hold, 2 °C/min ramp	17
	135 μm	Pentaerythritol tetraacrylate (PETA), divinylbenzene (DVB), PEGDA	Energy storage, catalysis, adsorption	900 °C final, 300 °C air hold, 880 °C CO2 hold	34
	20 μm	Boston Micro-Fabrication HTL yellow resin	Scaffold for cell growth	900 °C final, 350 °C isothermal hold, 3 °C/min ramp	68
	200 μm	PIC100 (EnvisionTEC) with graphene oxide	Semiconductors	500 °C final, 150 °C, 300 °C, and 400 °C holds, 2 °C/min ramp	69
	700 μm	Sartomer SR-339, ZIF-8 MOF	Heterogeneous catalysis and ferromagnetism	950 °C final, 3 °C/min ramp	70
	~500 μm	VisiJet FTX Green	Electrodes for Biomedical Engineering	850 °C final, 300 °C hold	71
	mm scale	Arkema Sartomer SR238, SR295	Electrochemical Applications	900 °C final, 30 and 400 °C holds, 2 °C/min ramp	72
Digital light processing (DLP)	133 μm	Elegoo	High Capacitance MnO$_2$ Supercapacitors	1000 °C final, 900 °C CO$_2$ hold	37
	200 μm	Elegoo	Polymer electrolyte membrane fuel cells	900 °C final, 10 °C/min ramp	73
	200 μm	Elegoo	Structural Energy Storage Applications	1000 °C final, 400 °C hold, 10 °C/min ramp	74
	33 μm	Elegoo	Sodium Ion Batteries for Energy Storage	1000 °C final, 400 °C hold, 10 °C/min ramp	75

Table 1. continued

AM Method	Pyrolyzed Material Feature Size	Application	Resin	Furnace Conditions	Reference
	117 µm	Microbial Fuel Cell	Miicraft 200ST	800 °C final, 350 and 450 °C hold, 1.5–3 °C/min ramp	15
	28 µm	Electrodes for Energy Storage	PR48	1000 °C final, 300 and 400 °C hold, 5 °C/min ramp	32
	106 µm	High Strength Structural Applications	PR48	1000 °C final, 300 and 400 °C hold, 10 °C/min ramp	76
	60 µm	High Strength Structural Applications	PR48	1000 °C final, 300 and 400 °C hold, 10 °C/min ramp	13
	300 µm	Microsupercapacitors for Redox Reactions	Allnex Ebecryl 265	430 °C final, 150 °C hold	77
Projection micro stereolithography (PµSL)	~10 µm	Aerogel foams, energy storage, separations, catalysis	PEGDA, bisphenol A ethoxylate dimethacrylate (BisA-EDMA), graphene oxide	1050 °C final, 1 °C/min ramp	52
	25 µm	Lithium-Ion Batteries for Energy Storage	PR48	1000 °C final, 300 °C air hold, 400 and 600 °C N₂ hold, 2 °C/min ramp	19
Continuous liquid interface production (CLIP)	15 µm	Energy materials	PR48	800 °C final in N₂, 300 °C hold in air, 5 °C/min ramp	This work (see Section 6)

to the ability of these light-based printing techniques to achieve micrometer and nanometer feature sizes conducive to isotropic shrinkage and maintaining structural integrity during pyrolysis. DLW-2PP has been used to achieve the highest resolution features, down to 100 nm,[64] but method is magnitudes slower (10^{-9}–10^{-3} mm³/s) than projection stereolithography methods such as PµSL (1 mm³/s) and CLIP (10^3 mm³/s).[57] Most DLW-2PP studies have primarily used acrylate-based Nanoscribe resins for high strength, biosensing, and optics applications. Several of these investigations only conducted low temperature heat treatments (<600 °C) which begins the pyrolytic restructuring mechanisms of constituent polymeric materials but does not facilitate significant levels of carbon graphitization and conductivity, instead relying on additives such as MOFs[62] and zirconium[61] or electroforming after pyrolysis.[63] Other DLW-2PP studies investigating higher temperature pyrolysis for structural applications achieved among the highest strength values observed for pyrolyzed 3D printed structures, for example Desponds et al.[64] reported up to 1 GPa for a pyrolyzed zirconia and acrylate-base material and Bauer et al.[12] reported reaching 3 GPa for an IP-Dip honeycomb structure. However, these pyrolyzed structures with extremely fine features and high strength produced via DLW-2PP were less than 100 µm wide in total length due to small build area capabilities, indicating that this method would be time-intensive for generating macroscale load-bearing structures.

For laser-based SLA, there is less consensus on commonly used resin precursors. Pan et al. demonstrated one of several instances of pyrolyzing SU-8 microstructures on silicon substrates, revealing a significant increase in anodic peak current and electrochemically active surface area (ECSA) for 3D printed electrodes versus 2D counterparts.[66] Toward electrode production, Steldinger et al. utilized a custom acrylate and aromatic vinyl-based carbon resin that undergoes CO_2 activation to achieve porous carbon structures with surface areas of 2200 m²/g.[34] Blyweert et al. combined acrylate components with mimosa tannin extract to produce pyrolytic carbon with thicker features (>4 mm) and mechanical strength of 215 MPa, but this system has not yet been shown to produce microscale features.[72] Tian et al.[71] used commercial VisiJet FTX Green resin to produce flexible carbon electrodes for skin biosensing applications for *in vivo* electromyography with areal capacitance of 8.9 mF/cm² and impedances at 1 kHz of around 2.5 kΩ, but they only produced flat structures that undergo significant warping and distortion.[71]

In the pattern projection light-based 3D printing space, DLP has been commonly used with commercial resin PR48, Elegoo, and other acrylate-based commercial resins to demonstrate feature sizes on a scale of 10–100 µm. Using PR48 resin, Narita et al. demonstrated the first instance of using DLP and pyrolysis to produce battery electrodes, achieving 28 µm carbon feature sizes, compressive strength of 27 MPa and specific strengths of 101 kN m/kg.[32] Kudo et al. produced high strength pyrolytic carbon out of PR48 lattice structures that achieve up to 389.57 MPa in compressive strength and 468.62 MPa cm³/g in specific strength.[13,76] Using a liquid-crystal version of DLP and Elegoo resin, Katsuyama et al. showed that 3D printed pyrolytic carbon electrodes can facilitate the swift diffusion of carrier ions as anodes for sodium ion batteries (SIBs) and that reducing the diameter of the microscale lattice beams significantly improves rate performance and specific capacity.[75] They achieved SIB active material mass loading of

98 mg/cm^2 and areal capacity of 21.3 mAh/cm^2.[75] Kudo et al. included magnesium-oxide nanoparticles as porogens in Elegoo resin to generate carbon with hierarchical porosity including macropores (~5 μm), mesopores (~50 nm), and micropores (~1 nm) with areal capacitance of 10 F/cm^2 and gravimetric capacitance of 105 F/g but lower mechanical strength compared to samples without MgO.[74] Large area PμSL, another recent VP method, has been used by Hensleigh et al. to produce microarchitected graphene aerogels from a custom acrylate resin with features sizes on the order of 10 μm with 60 nm pores that contributed to a surface area of 130 m^2/g.[52] Reale Batista et al. used large area PμSL with PR48 to generate electrodes for lithium-ion batteries.[19] The large area and high resolution capabilities offered by PμSL particularly make it a compelling 3D printing method for carbon microstructure generation. Additionally, Section 6 of this perspective demonstrates the use of highly scalable CLIP VP alongside pyrolysis of PR48 resin to produce pyrolytic carbon lattices with 15 μm beam diameters.

These investigations advance the understanding of structural and material considerations for generation of pyrolyzed 3D printed structures. Of the methods overviewed, VP processes benefit most from inherent scalability enabling mass production of 3D pyrolytic carbon designs at length scales from cm to μm. Ultimately, for all 3D printing methods described herein, more promise arises with custom designing a resin tailored for optimal pyrolysis outputs rather than using existing commercially available resins not initially designed for pyrolysis.

3. MOLECULAR DESIGN STRATEGIES FOR POLYMERIC 3D PRINTING RESINS

A variety of commercial resins have been used in 3D printing and pyrolysis processes to produce 3D carbon structures; most are either acrylate or epoxy-based (Table 2). Acrylate monomers are commonly used due to their affinity for undergoing radical polymerization during AM.[80]

Several commercially available resins, such as PR48,[19,32,36] EnvisionTEC PIC100,[69] and Elegoo resins,[37] yield conductive carbon after pyrolysis, but they typically undergo substantial linear shrinkage of up to 70−90%. Achieving higher carbon yields leads to less shrinkage, which is desirable for material retention. Besides the challenges associated with geometry retention and char yields, pyrolytic carbon derived from commercially available resins often exhibits only modest electrical conductivity.[1,15,19,81] Modifications such as incorporating graphene oxide[19] and tethering aromatic polymer precursors[82] have been made to commercial resins to increase carbon content after pyrolysis, but these systems still have extraneous components in their composition that do not contribute to the carbon output.

Insights gained from the compositions of these commercial resins have been used to inform the development of custom resins designed specifically for high char yield pyrolysis output. (Table 3). The pyrolytic carbon structures resulting from these custom resin systems vary in shape and pore morphologies (Figure 3). We have grouped the structures into those that demonstrate high char yields ≥50 wt % (Figure 3A−D), those that report mechanical strength >100 kPa (Figure 3D,E), and those with high resolution features <100 μm (Figure 3F,G). Additionally, we highlight systems that incorporate important resin components including polyacrylonitrile (Figure 3H,I), biomass (Figure 3J−L), and MOFs (Figure 3M,N).

Table 2. Composition and Characteristics of the Commercial 3D Printing Resins That Have Been Used in Tandem with Pyrolysis to Generate Conductive Pyrolytic Carbon Structures

Commercial Resin Name	Commercial Resin Composition (Including Percentages When Provided)	AM Methods	Highest Resolution Pyrolyzed Feature	References
PR48	Acrylate-based: Allnex Ebecryl 8210 (39.8 wt %), Genomer 1122 (19.9 wt %), Sartomer SR 494 (39.8 wt %), 2,4,6-Trimethylbenzoyl-diphenylphosphineoxide (TPO, 0.4 wt %), Mayzo OB+ UV blocker (0.16 wt %), and undisclosed aliphatic urethane acrylate	DLP, PμSL, CLIP	15 μm	32, 13, 76, 19, this work
Elegoo	Acrylate-based: trimethylcyclohexyl acrylate (53%), Isopropylidenediphenol (26%), (5-ethyl-1,3-dioxan-5-yl)methyl acrylate (14%), Ethyl phenyl (2,4,6-trimethylbenzoyl)phosphinate (5%), titanium dioxide (1.5%), carbon black (0.5%)	DLP	33 μm	37, 74, 75
Kayaku Advanced Materials SU-8	Epoxy-based: epoxy novolac resin with average epoxide group functionality of 8 (no wt % provided)	SLA	2 μm	17, 66, 67
IP-Dip (Nanoscribe GmbH)	Acrylate and polyether-based: aliphatic alcohol acrylate (60−80%), alicyclic hydrocarbon with acrylate and polyether components (<24%), additional hydrocarbon acrylate (<24%)	DLW-2PP	250 nm	36, 63, 65, 12
Boston Micro-Fabrication HTL yellow resin	Acrylate-based: Tris[2-(acryloyloxy)ethyl] isocyanurate (5−40%), Acrylic Ester (20−80%), 4-(1-oxo-2-propenyl)-Morpholine (10−30%)	SLA	15 μm	68
IP-S (Nanoscribe GmbH)	Acrylate-based: methacrylate carbamate mixture (>95%), butyrolactone (<5%), aromatic ketone photoinitiator (<1%)	DLW-2PP	100 μm	58
VisiJet FTX Green	Acrylate-based: Triethylene glycol diacrylate (40−55%), Tricyclodecane dimethanol diacrylate (15−25%), TPO (1.5−2.5%)	SLA	500 μm	71
PIC100 (EnvisionTEC)	Acrylate-based: Methacrylated oligomer (50−90%), methacrylated monomer (5−40%), phosphine oxide photoinitiator (1−2%)	SLA	200 μm	69
Miicraft 200ST	Acrylate-based: acrylate compounds (90−98 wt %), photoinitiator (2−10 wt %), additives (0.2−5 wt %); no further details provided	DLP VP	117 μm	15

Table 3. Custom 3D Printing Resins Developed for Pyrolysis to Generate Conductive Carbon Structures[a]

Highest Resolution Feature	Custom Resin Components with Percent Composition (wt %) when Provided	3D Printing Method	Char Yield	Application	Reference
250 μm (Figure 3A)	· Cellulose nanocrystals (162.5 g/mL suspension in water; 67.9%) · ZIF-8 metal−organic framework (MOF) (32.1%)	DIW	50%	Energy Storage	60
500 μm (Figure 3B)	· Pyromellitic dianhydride with 4,4′-oxidianiline (PMDA-ODA) (18−24%) · TPO photoinitiator (2.5%) · N-methyl-2-pyrrolidone solvent (remainder of composition)	DIW and SLA	75%	Energy applications	82
mm scale (Figure 3C)	· Poly(4-vinylphenol)-plutonic F127 in a 2:1 by mass ratio (36.3%) · Activated carbon (48.5%) · Bentonite binder (15.1%)	DIW	58%	Gas Separation, adsorption of CO_2	59
>100 μm (Figure 3D)	· Phthalonitrile (55 wt %) · Bisphenol A ethoxylate diacrylate (BisA-EDA) (small undisclosed amount) · DMF solvent (remainder)	PμSL	64%	Energy, electrochemistry, and aerospace	83
135 μm (Figure 3E)	· Pentaerythritol tetraacrylate (PETA) (1:1 volume ratio with DVB, with the monomer mixture being 50 vol % total) · Divinylbenzene (DVB) (1:1 volume ratio with PETA) · DEP porogen (50 vol %)	DLP	48%	Energy storage, catalysis, and adsorption	34
10 μm beams, 60 nm pores (Figure 3F)	· Bisphenol A ethoxylate dimethacrylate (BisA-EDMA) (Cumulative 12 wt % with PEGDA) · Polyethylene glycol diacrylate (PEGDA) (Cumulative 12 wt % with BisA-EDMA) · Graphene oxide (GO) (1 wt %) · Photoinitiator (2−4 wt %) · N,N-Dimethylformamide (DMF) solvent (remainder of composition)	PμSL	40−50%	Energy storage, separations, catalysis	52
25 μm (Figure 3G)	· Trimethylolpropane triacrylate (TMPTA) (95 wt %) · GO (3 wt %) · Phenylbis (2,4,6-trimethylbenzoyl) phosphine oxide (2 wt %)	PμSL	17%	Energy storage	19
mm scale (Figure 3H)	· Polyacrylonitrile (PAN) (90 mol %) · Solketal acrylate (SKA) (10 mol %) · DMSO and methanol solvents	FFF	77% by volume	Energy Storage	43
500 μm (Figure 3I)	· Poly(n-butyl acrylate) with trithiocarbonate terminus (PBA-CTA) (28.8 wt %) · Acrylonitrile (54.9−66.4 wt %) · TMPTA (0.8−15.3 wt %) · TPO photoinitiator (1.0 wt %) · Sudan II UV blocker (0.03 wt %)	LCD VP	40%	Energy Storage	84
700 μm (Figure 3J)	· Microfibrillated cellulose hydrogel (1.6%) · Lignosulfonate (76.6%) · Cellulose powder (CP) from cotton (21.8%	FFF	Up to 50%	Energy Storage	44
400 μm (Figure 3K)	· Hydroxypropyl methylcellulose (5%) · GO (40 mg/mL suspension in water, 95%)	DIW	No mention	Energy Storage	45
500 μm (Figure 3L)	· Starch-based packaging waste (20%) · Sodium hydroxide (80%)	DIW	No mention	Energy Storage	85
700 μm (Figure 3M)	· 2-Phenoxyethyl acrylate (41.4 wt %) · TMPTA (41.4 wt %) · ZIF-8 MOF (5 wt %) · Ni-BTC MOF (5 wt %) · Photoinitiator (7.2 wt %)	SLA	11%	Catalysis	70
mm scale (Figure 3N)	· Mimosa tannin extract (25 wt %) · Acrylate resins (HDDA, PETA) (74.7 wt %) · ZIF-8 MOF (0.3 wt %)	SLA	22%	Electrochemistry	72

[a]Resin compositions are listed as reported or calculated from methods sections.

Developing an effective formulation for 3D printing polymeric structures that can be pyrolyzed to graphitic carbon with high-resolution features (<10−100 μm), high char yield (>50 wt %), good conductivity (>1 S/cm), and structural integrity (strength >100 kPa, no distortion) relies on intentionally tailoring the molecular structure of the constituent components. Polymer components used in literature to achieve high char yields have primarily consisted of functional groups that either contain 6-membered carbon rings, for example aromatics, or stabilize via cyclization to 6-membered carbon rings during the pyrolysis process, for example nitrile groups. Aromatics, such as phenyl or naphthyl groups, provide stability to the carbon structure and are less likely to decompose into volatile compounds, resulting in a higher
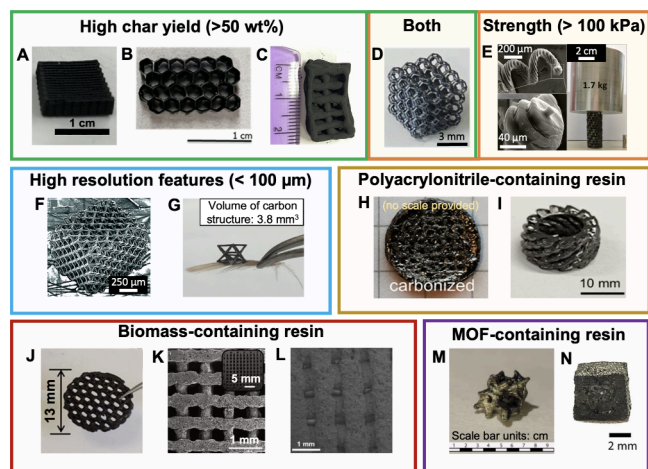
Figure 3. Carbon structures produced via 3D printing of custom polymer systems followed by pyrolysis corresponding to the Table 3 studies. These structures are grouped into high char yield samples (green), samples reporting mechanical strength (orange), samples with high resolution features (blue), and samples produced from polyacrylonitrile-containing resins (gold), biomass-containing resins (red), and MOF-containing resins (purple). These optical and SEM images are reproduced (adapted) with permissions when necessary from (A) Catarineu et al.[60] Copyright 2023 Elsevier, (B) Arrington et al.[82] Copyright 2021 American Chemical Society, (C) Comroe et al.[59] CC BY, (D) Lu et al.[83] Copyright 2024 Elsevier, (E) Steldinger et al.[34] CC BY, (F) Hensleigh et al.[52] CC BY-NC, (G) Reale Batista et al.[19] Copyright 2023 Elsevier, (H) Usselmann et al.[43] CC BY, (I) Bobrin et al.[84] CC BY, (J) Shao et al.[44] Copyright 2018 Elsevier, (K) Yao et al.[45] Copyright 2019 Elsevier, (L) Idrees et al.[85] Copyright 2020 Elsevier, (M) Cherevko et al.[70] CC BY, and (N) Blyweert et al.[72] CC BY.

char yield.[86] Nitrile groups can stabilize the polymer structure during pyrolysis by participating in the formation of stable nitrogen-containing cyclic compounds during the heating procedure.[87] This mitigates the decomposition of polymer into volatile gases during pyrolysis, increasing char content.

Several components that have been incorporated into 3D printed polymer formulations that have shown promise for pyrolysis to carbon are included in Figure 4. These molecular structures have been separated into acrylate-based cross-linker monomers typically used in VP 3D printing, monomers that increase pyrolysis char yield, comonomers that improve formulation printability, and nonpolymerizing additives that increase char yield.

3.1. High Char Yield

Focusing first on high char yield resins, often these materials are highly cyclic compounds such as biomass-containing materials or polyimides, often with additives included to bolster mass yield. Catarineu et al. developed a cellulose-based resin for DIW with ZIF-8 MOF additives to produce a carbon cathode with >50 wt % char yield for a zinc-ion hybrid supercapacitor (Figure 3A).[60] After pyrolysis at 1000 °C, this material underwent graphitization and achieved surface areas of 660 m^2/g, but demonstrated low-resolution lattice features due to the DIW nozzle being 600 μm. Other biomass-containing studies that did not report char yield are discussed later. Arrington et al. achieved a char yield of 75 wt % by developing an SLA resin with polyimide pyromellitic dianhydride with 4,4′-oxidianiline (PMDA-ODA), poly(amic acid) salts, and solvent pyrolyzed at 1000 °C to produce

carbon with high conductivity over 1 S/cm (Figure 3B).[82] During Raman spectroscopy, their rigid 3D organogels displayed D and G bands characteristic of polycrystalline pyrolytic carbon.[82] Comroe et al. achieved a high char yield of 58 wt % by incorporating activated carbon particles into poly(4-vinylphenol) in N,N-dimethylacetamide solvent.[59] After FFF and pyrolysis at 800 °C, this formulation generated structures that demonstrated viability for gas separation applications but were printed with mm-scale resolution and underwent significant deformation (Figure 3C). Lu et al. printed structures with features on the 100 μm scale that achieved 62% char yield using phthalonitrile, containing both aromatic and cyclization-prone nitrile groups, along with cross-linker BisA-EDA via PμSL (Figure 3D).[83]

3.2. Mechanical Integrity

Looking to mechanical strength, the phthalonitrile structures printed by Lu et al. also demonstrated storage modulus of 3.7 GPa and flexural strength of 156 MPa.[83] Steldinger et al. produced hierarchically structured porous carbon (Figure 3E) strong enough to withstand crushing pressures up to 100 kPa via custom resin formulations with monomers that included PETA, DVB and PEGDA and dibutyl phthalate as a porogen. Due to its high degree of aromaticity, DVB enabled char yields up to 48% at 900 °C, but electrochemical characterization was not reported and the resin required long solidification times of 240−420 s per layer.[34] Limited studies report mechanical properties, indicating a need for the field to generate tougher structures and more widely report mechanical characterization.

3.3. High Resolution Features

PμSL VP printing was used in two custom resin studies to achieve high resolution features <100 μm. Hensleigh et al. developed a resin that combines BisA-EDMA, which alone pyrolyzes to brittle char, and PEGDA (700g/mol), which alone produces a mechanically weak gel, in a 1:1 weight ratio in DMF solvent to produce a robust carbon aerogel after pyrolysis (Figure 3F).[52] Their microarchitected graphene aerogel lattices demonstrated beam diameters on the order of 10 μm and attained mechanical elastic modulus normalized by material density comparable to graphene.[52] Reale Batista et al. incorporated GO sheets into TMPTA resin that they printed using PμSL and pyrolyzed in N$_2$ up to 1000 °C after several isothermal holds (Figure 3G).[19] These GO/TMPTA lattices achieved significantly greater gravimetric capacitance than analogous commercial PR48 samples. PμSL and similar high resolution VP 3D printing techniques have demonstrated the most promise for achieving desired high-resolution features.

3.4. Polyacrylonitrile-Based Resins

Looking to the carbon fiber industry history (Figure 1), one of the most widely used materials in pyrolysis is PAN.[88] The pyrolysis of PAN to conductive carbon via cyclization of linear chains has been extensively studied and is promising for use in conductive electrode applications.[87,89] In particular, there has been a recent push in late 2023 and 2024 for inclusion of polyacrylonitrile into new 3D printing resin systems for pyrolysis. Usselmann et al. demonstrated a FFF method copolymerizing PAN with solketal followed by pyrolysis to generate open mesh carbon electrodes for supercapacitors (Figure 3H).[43] However, this melt extrusion method printed features on the mm scale rather than μm scale, which limits the achievable high end S$_V$. A study by Chazot et al. introduced a
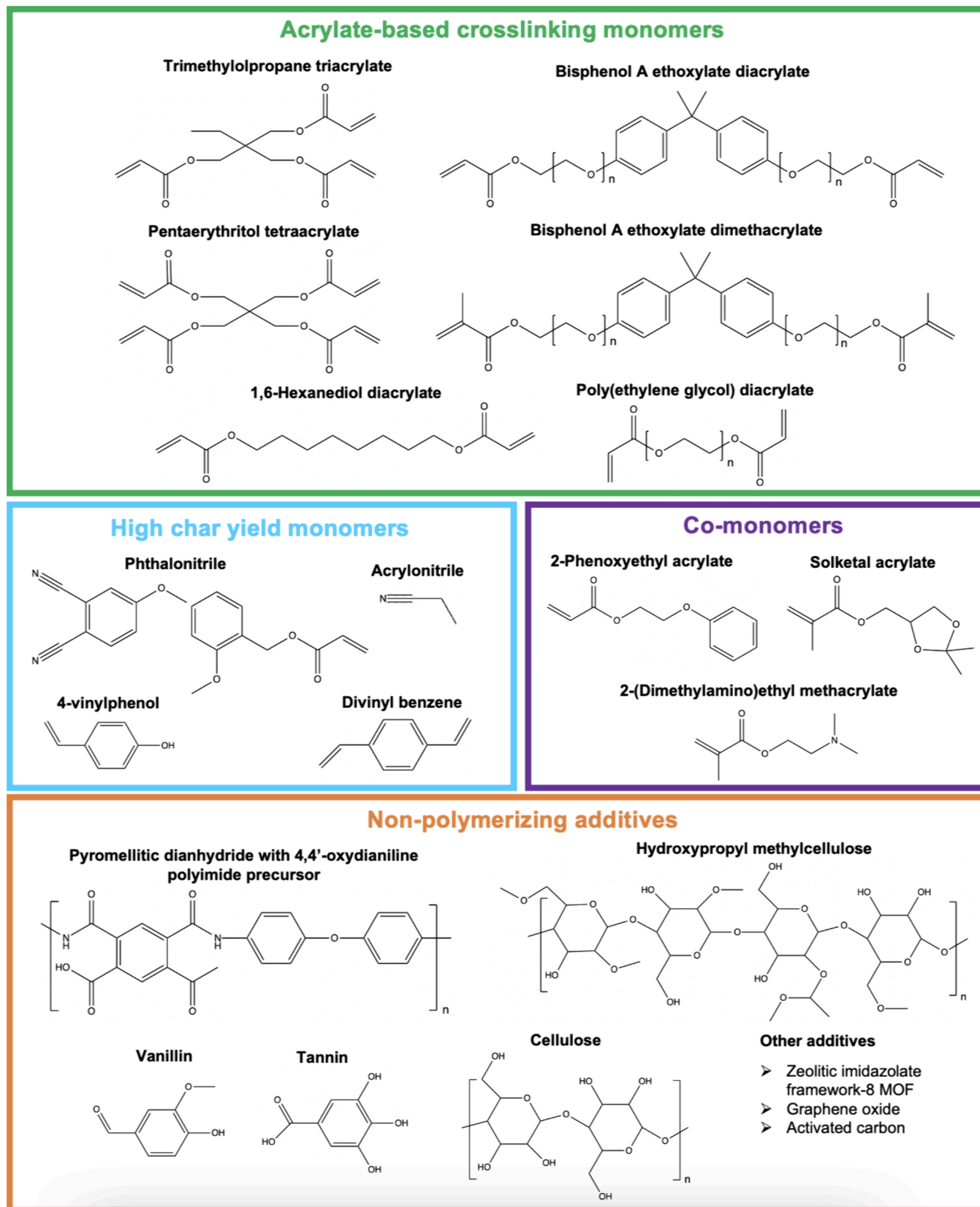
Figure 4. Molecular structures of several components used in 3D printing polymer resins designed for improved pyrolysis output.

new strategy for 3D printing PAN using an interfacial vat photopolymerization method but has not yet been combined with pyrolysis.[90] In 2024, Bobrin et al. demonstrated

generation of pyrolyzed PAN-based structures via VP 3D printing for the first time (Figure 3I), using a solvent-free microphase separated resin comprising of a sacrificial polymer
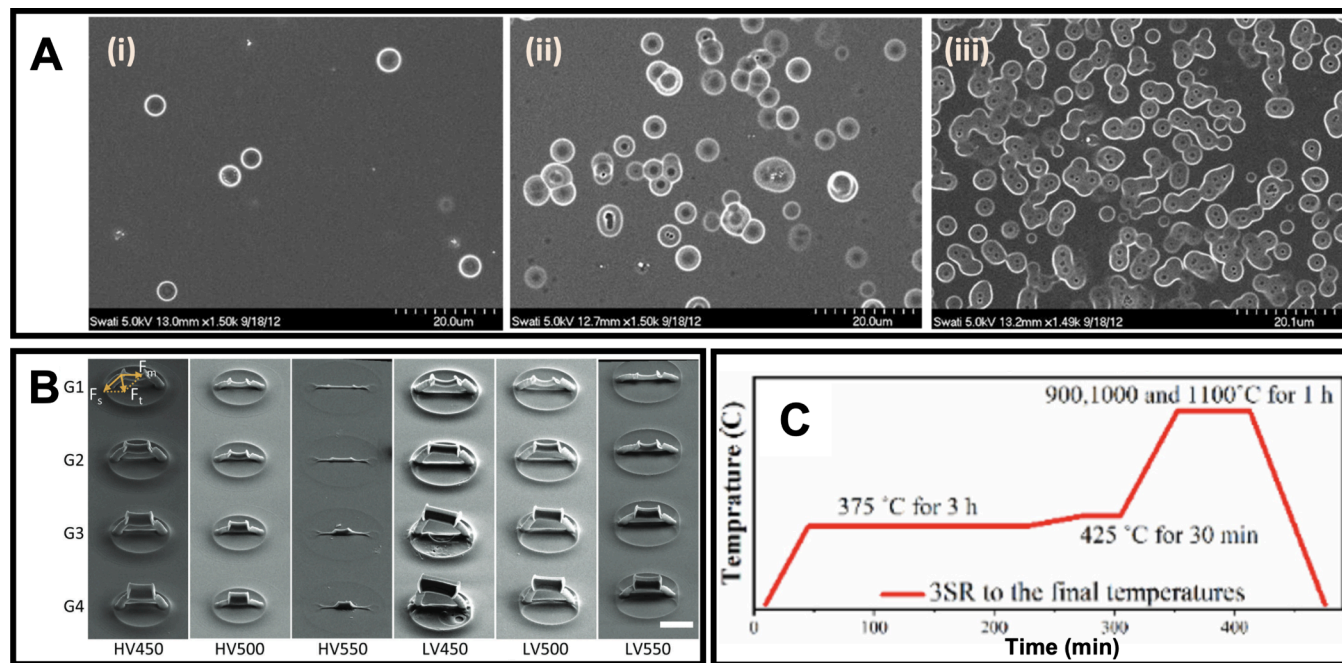
Figure 5. Pyrolysis condition effects on structure including (A) pyrolyzed SU-8 material after undergoing heating rates of (i) 25 °C/min, (ii) 50 °C/min, and (iii) 75 °C/min demonstrating more gas pockets forming at higher ramp rates (Reproduced with permission from Sharma reproduced with permission from Sharma et al.[101] Copyright 2014 Elsevier), (B) beams of higher thicknesses, lower S_v, and high vacuum (HV) experiencing less warping during pyrolysis than smaller thicknesses and low vacuum (LV)[36] (CC BY-NC), and (C) the temperature profile of a furnace run with isothermal holds[81] (CC BY-NC-ND).

poly(*n*-butyl acrylate) with a trithiocarbonate terminus, TMPTA, and carbon precursor acrylonitrile.[84] After pyrolysis at 1200 °C, they produced structures with mm-scale printed features and nanoscale porous texture that achieved conductivity of 0.025 S/cm.[84] Bobrin et al. have also used this pyrolyzed 3D printed PAN microphase chemistry in a recent carbon-ceramic system.[91] However, no existing VP literature demonstrates generation of PAN structures with <100 μm printed features, which is a key target area for future work due to the affinity for PAN for pyrolysis of highly graphitic carbon.

3.5. Biomass-Based Resins

Several more studies include biobased components, for example, Shao et al. incorporated cellulose and lignosulfonate into FFF filament to generate electrode disks with 700 μm features (Figure 3J)[44] and Yao et al. incorporated hydroxypropyl methylcellulose into a graphene oxide DIW ink to produce cubic lattice electrodes with 400 μm beams (Figure 3K).[45] The Shao et al. carbon structures demonstrated electrical conductivity of 47.8 S/cm.[44] Alternatively, Idrees et al. produced FFF resin consisting of starch-based packaging waste with sodium hydroxide for solid-state supercapacitor electrodes (Figure 3L).[85]

3.6. MOFs and Other Nonpolymerizing Additives

In addition to tailoring the polymer backbone, numerous studies have increased the char yield, porosity, surface area of their pyrolytic carbon structures by incorporating nonpolymerizing additives into the resins, for example MOFs. In 3D printing and pyrolysis literature, the MOF usually incorporated is zeolitic imidazolate framework ZIF-8 due to its low cost, water stability, and compatibility with zinc ion capacitor systems.[60] Blyweert et al. added ZIF-8 MOF into an acrylate-based resin comprised of HDDA and PETA mixed with mimosa tannin extract, yielding low density carbon

structures after pyrolysis at 900 °C that exhibit electrical conductivity of 7 S/cm (Figure 3N).[72] Blyweert et al. later improved this approach to achieve a 27% char yield by integrating vanillin with tannin into the acrylate polymer network, which improved thermal stabilization and decreased the depolymerization of free chains in the polymerized resin.[40] Cherevko et al. incorporated ZIF-8 and the nickel-based Ni-BTC MOFs into TMPTA and 2-phenoxyethyl acrylate resin for SLA printing of structures for nickel-based catalysis.[70] After pyrolysis at 950 °C, their structures (Figure 3M) demonstrated isotropic shrinkage, surface areas of 145 m^2/g, and magnetic coercivity of 36 Oe, on the order of nickel metal. Catarineu et al. also utilized ZIF-8 as described above and showed via elemental analysis that the zinc introduced by ZIF-8 additives volatilizes at temperatures greater than 1000 °C.[60] Together, these studies have shown that MOFs can enhance the porosity, surface area, and electrochemical properties of 3D-printed carbon structures.

Outside of MOFs, other nonpolymerizing additives added to custom 3D printing resins have included porous activated carbon particles[34,59,85] and GO[69] to enhance conductivity. Hensleigh et al. and Reale Batista et al. both incorporated GO into their PμSL resins as mentioned above to enhance the porosity and gravimetric surface area of their structures (Figure 3E-F).[52] Yao et al. incorporated GO into their hydroxypropyl methylcellulose resulting in graphene aerogel structures with surface area of 100 m^2/g after pyrolysis at 1050 °C with high loading capacity for MnO$_2$ active material at 182.2 mg/cm^2 (Figure 3J).[45] The choice of additive to complement polymer resin composition plays a pivotal role in the outputted surface area and strength of a material. Commonly, these additives add to the porous nature of the outputted carbon, increasing material surface area and resulting conductivity, but decreasing the mechanical strength.

Table 4. Overview of Pyrolysis Parameters and Furnace Conditions Used in Combination with Resins Used in Conductive Carbon Production

Resin	Ramp Rate (°C min⁻¹)	Pyrolysis Temperature (°C)	Pyrolysis Atmosphere	Pyrolysis Time	Char Yield (wt %)	Linear Shrinkage (%)	Electrical Conductivity	Reference
Commercial Resins								
IP-DIP	3	900	Vacuum	1 h	20%	80%	Not Reported	12
	1200	450−550	Vacuum	Not Reported	Not Reported	70%	Not Reported	36
	1200	450−550	N$_2$	Not Reported	Not Reported	55% - 68%	Not Reported	36
Elegoo	Not Reported	1000	Vacuum	2 h	Not Reported	66% - 67%	Not Reported	37
PR48	2	190 postcure; 300 in Air; 1000 in N$_2$	N$_2$	1 h; 3 h; 1 h	16%	30%	5 Ω (EIS)	19
	10	1000	Vacuum	4 h	~4%	66%	Not Reported	13
	5	1000	Vacuum	4 h	~5%	66%	Not Reported	32
	5	300 in Air; 800 in N$_2$	N$_2$	3 h; 2 h	16%	65%	Not Reported	This work; see Section 6
PR48 with titanium(IV) ethoxide	2	1000	Ar	1 h	25.80%	39%	Not Reported	108
FullCure 705	1	1000	N$_2$	2 h	16.5% - 22.3%	N/A	Not Reported	35
	1	1000	N$_2$	2 h	15.2% - 19.7%	N/A	Not Reported	35
Formlabs HTR	10	1000	N$_2$	1 h	7%	60% - 62%	25 Ω (From EIS)	81
Clear 2005T	0.4−3	800	N$_2$	2 h	7%	43%	23 Ω (From EIS)	15
SU-8	5	1200	Vacuum	N/A	Not Reported	N/A	Not Reported	104
Custom Resins								
GO/TMPTA	2	1000	N$_2$	1 h	17%	19%	6 Ω (From EIS)	19
CN154/PETA/HDDA/BAPO	1−2	900	N$_2$	1 h	28%	25%	Not Reported	40
	1.5−2.5	900	N$_2$	1 h	21%	25%	7 S cm⁻¹	39
	1.5−2.5	900	N$_2$	1 h	11.70%	40%	Not Reported	39
PEGDA/PETA/DVB	3.3	900	N$_2$	15 min	48%	35%	Not Reported	34
GO/PEGDA/BisA-EDMA	1	1050	N$_2$	3 h	40% − 50%	50% − 60%	64 S m⁻¹	52
ZIF-8/2-Phenoxyethyl acrylate/TMPTA	3	950	H$_2$, 7.03 vol % Ar	5 min	11%	50%	Not Reported	70
Poly(4-vinylphenol)/ Pluronic F127/activated carbon/bentonite	10	900	N$_2$	N/A	58%	N/A	Not Reported	59
PAN/Solketal acrylate	0.5−5	1000	N$_2$	30 min	Not Reported	23%	~9 Ω (From EIS)	43
GO/hydroxypropyl methylcellulose	2	1050	N$_2$	3 h	Not Reported	Not Reported	~1.2 Ω (From EIS)	45
ZIF-8/cellulose nanocrystals	5	1000	N$_2$	2 h	50%	<10%	~5 Ω (From EIS)	60
Microfibrillated cellulose/ lignosulfonate/cellulose powder	0.2−1	600−1000	N$_2$	10 min	40% − 45%	41% − 48%	47.8 S cm⁻¹	44

4. PYROLYSIS CONDITIONS AND GEOMETRY PARAMETERS

During pyrolysis of polymeric structures, gaseous byproducts such as CO, CO_2, hydrocarbons, and H_2O[65,92−94] are formed and liberated at high temperatures, leaving behind a carbon skeleton comprised of fused ring structures of sp^2 hybridized carbon commonly accompanied by disordered defects and sp^3 hybridization.[36,95,96] The molecular behavior during the pyrolysis process can be categorized into three stages: monomer evaporation and cyclization, chemical decomposition, and carbonization.[49] This process must be controlled to maximize the graphitic yield for high conductivity and robust mechanical integrity, and to minimize geometric distortions. Several polymer pyrolysis methods exist beyond traditional tube furnace pyrolysis, such as fast joule heating,[13,97] rapid thermal processing via IR lamps,[86] microwave-assisted pyrolysis,[98] and inductive heating.[11] These nontraditional methods involve rapid heating to a final temperature and are commonly used in the pyrolysis of biomass and waste plastic,

where retention of a specific part geometry is not necessary. The focus of this section is therefore limited to the parameters of conventional tube furnace pyrolysis, namely temperature ramp rates, maximum pyrolysis temperature, chamber pressure, and atmosphere, and their effect on the properties of pyrolytic carbon generated from 3D printed polymer resins.

Polymer degradation to carbon usually occurs between 300 and 550 °C, as volatile byproducts form and diffuse out, leaving behind a disordered carbon-rich framework.[36,96,99,100] Rapid heating rates can cause the formation of byproducts to outpace their diffusion out of the polymer network, causing pockets of gas to become trapped in the bulk or on the surface of the carbon matrix (Figure 5A).[96,101] Fast heating rates also prevent adequate relaxation of internal stresses developed in the polymer during the printing process, contributing to structural distortions in the printed parts.[19,36,102]

Key structural changes impacting electrical conductivity and mechanical strength of pyrolytic carbon are determined by the final pyrolysis temperature and dwell time. Cleavage of hydrogen from carbon, heteroatom liberation from the carbon matrix, the cyclization of nonaromatic components, and compactification and rearrangement of C−C bonds in sp^2-hybridized domains during the pyrolysis are all impacted by the maximum temperature and dwell time.[16,95,96,102] Between 550−700 °C, after the primary thermochemical degradation of the polymer, the remaining disordered carbon material contains a high fraction of unsaturated dangling bonds and active radicals.[103] At temperatures above 700 °C, hydrogen, nitrogen, and any remaining oxygen are expelled and the aromatic network becomes interconnected, increasing the stacking thickness and in-plane crystallite size of the newly formed graphene-like structures.[99,100,104] Pyrolysis at temperatures above 800 °C has been observed to increase the modulus, hardness, and electrical conductivity compared to pyrolysis at lower temperatures due to enabling increased carbon content.[16,96] For example, after pyrolysis of SU-8, at 900 °C, the elemental composition of the material reports 90 wt % carbon content by mass whereas when the pyrolysis temperature is increased to 1300 °C, the carbon content reaches 99 wt %.[100] The formation of gaseous byproducts and the coalescence of the aromatic network are primarily responsible for the large volume changes observed in pyrolyzed polymers.

The chamber pressure and atmosphere during pyrolysis affects both the rate of outgassing of byproducts, which can cause second-order reactions with the carbon backbone, and the rate of heteroatom diffusion within the polymer during the polymer-carbon conversion.[36,99] Vacuum conditions have been shown to enable the formation of higher molecular weight byproducts compared to ambient pressure.[105] Low chamber pressure in vacuum pyrolysis enhances the transport of volatile byproducts within the polymer, allowing their evacuation to occur at lower temperatures resulting in larger linear shrinkage (Figure 5B).[99] Samples undergo slower carbonization in inert atmospheres, such as argon (Ar) or nitrogen (N_2), compared with vacuum pyrolysis, as the slower outgassing of byproducts hinders the conversion of polymer to carbon. The use of inert carrier gases such as argon or nitrogen are common to avoid oxidation of carbon. Slower carbonization also occurs in an air or oxygen-containing atmosphere, which can also generate an oxygen-rich skin on samples pyrolyzed at high pressures. Compared with those pyrolyzed under vacuum conditions, the residence time for adsorbed oxygen-containing byproducts in

samples under pressure is higher, increasing the probability of second-order reactions.[36] In nonvacuum pyrolysis, using a gas with a high heat transfer coefficient, such as hydrogen (H_2), more readily transfers heat to the polymer, increasing the rate of byproduct formation which causes higher shrinkage and mass loss.[99]

To overcome challenges associated with geometric distortion during the polymer carbonization, researchers often include one or more isothermal stages at temperatures corresponding to significant polymer degradation prior to the final pyrolysis temperature (Figure 5C).[12,13,19,32,34] This allows for the controlled outgassing of byproducts while the material is still malleable prior to carbonization. Slow ramp rates, typically between or below 1−5 °C/min, are preferred to reduce geometric distortion and mass loss.[12,19,32,35,81,106] Since electrical conductivity is enhanced by an interconnected network of sp^2-hybridized carbon, final pyrolysis temperatures are typically above 900 °C with dwell times of 1 h or longer in inert or vacuum environments (Table 4). When reporting conductivity of carbon structures, most studies focus on device metrics and less on material properties of the carbon itself, as evidenced by less than half of the studies in Table 4 reporting material electrical conductivity. It is difficult to compare material properties when only device metrics are provided, so we recommend that the future papers in this field be more diligent about reporting carbon conductivity via electrochemical impedance spectroscopy.

Due to the dependence of shrinkage on the volatilization of side products, the S_V of printed parts becomes important. Higher S_V enables facile mass transport of volatile gases out of the polymer network due to corresponding with thinner diffusion pathways, thus higher S_V typically corresponds to more rapid and higher degrees of shrinkage.[36,107] However, Sun et al. observed that while this trend is consistently observed in low and no vacuum systems, the dependence of part shrinkage on S_V was not observed under high vacuum systems on a single-digit micron scale when using DLW-2PP 3D printing of IP-Dip.[36] Under high vacuum, beams with features between 1 and 4 μm exhibited similar shrinkage rates regardless of S_V (for example linear shrinkage of 45% at 450 °C and 30% at 500 °C). Conversely, under low vacuum (nitrogen atmosphere), beams with higher S_V underwent greater shrinkage, for example at 500 °C, beams with diameters of 1 μm, 2 μm, 3 μm, and 4 μm (decreasing S_V) underwent 32%, 39%, 42%, and 45% linear shrinkage.[36] Further investigation must determine whether this trend continues for larger features sizes ($\geq$100 μm scale), as more findings like these would enable nuanced control over outputted pyrolytic carbon feature sizes.

4.1. Future Outlook on Catalytic Graphitization of 3D Printed Structures

To utilize 3D printed carbon structures as conductive electrodes for energy storage and conversion, they must offer excellent conductivity and mechanical integrity. Pyrolysis to achieve graphitization is a critical step for achieving these properties. However, the conversion of carbonaceous precursors to graphitic carbon occurs at very high temperatures (>3000 °C).[109−111] One method for avoiding high temperatures that require significant energy to maintain is through catalytic graphitization, which is when polymers are converted with catalyst assistance into carbon nanomaterials, such as carbon nanotubes[112−115] and graphene,[116,117] through dis-
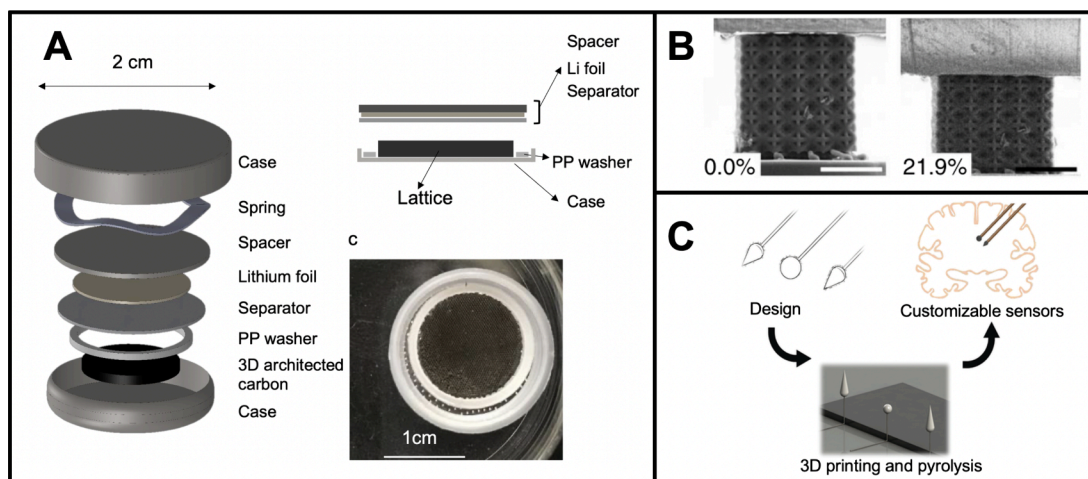
Figure 6. Diagrams showing example uses for pyrolyzed 3D printed structures in (A) an energy storage application with a carbon lattice being assembled into a Li-ion coin cell (from Narita et al.[32] Copyright 2021 John Wiley & Sons), (B) a structural application showing a carbon lattice undergoing 21.9% strain without breaking (from Crook et al.[10] CC BY), and (C) a biomedical application specifically targeting customizable neurotransmitter detection implants (from Yang et al.[58] Copyright 2018 John Wiley & Sons).

solution and precipitation mechanisms. Catalysts used in catalytic graphitization of polymers serve two functions: (1) facilitating effective degradation and volatilization of non-carbon elements and (2) enabling arrangement of graphitic carbon on the structure.[118−120] Similar to carbon nanotube synthesis by chemical vapor deposition method, the catalysts for carbonization are usually transition metals, such as nickel,[121] iron[122] or metal compounds like nickel oxides,[113] ferrocene[123] or ferrous chlorides.[124] Furthermore, conducting carbonization under high pressure environment can generate carbon materials with textured micro or nanostructures and a relatively high carbon yield compared to atmosphere carbonization.[125] Besides the selection of catalysts, other critical factors that may significantly affect carbonization results include heating rate of pyrolysis,[126] pressure[125] and the S_v of the structure. Incorporating catalytic graphitization into the pyrolysis of 3D printed polymers is a critical future focus for the field that has been underutilized to date to achieve desired graphitic carbon structures at lower energy costs.

5. APPLICATIONS FOR PYROLYSIS OF 3D PRINTED STRUCTURES

3D printed carbon structures have the potential to address several critical global climate change challenges including as electrodes for energy applications such as renewable energy storage devices (Figure 6A), as conductive components supporting electrification of petroleum-heavy thermochemical processes, and as substrates for electrocatalysts supporting recovery of resources from waste or CO_2 capture. They also show merit in lightweight mechanical applications (Figure 6B) and biomedical applications like biochemical sensing (Figure 6C). Their high surface area, electrical conductivity, and tunable surface chemistry make them ideal candidates for addressing pressing global climate change mitigation challenges.

5.1. Energy Storage

Intensive research has shown promise for using 3D architected electrodes in battery applications, as increasing electrode thickness enhances energy density.[1,127−130] Industry standard planar 2D electrodes are hindered by tortuous ion diffusion pathways, low electrical conductivities due to the inclusion of binders, and high mass fractions of inactive components like separators and current collectors.[37,131] 3D architected carbon electrodes can improve upon 2D electrodes through high surface area (approaching graphene surface area of 2800 m^2/g) and open structures to accommodate volume changes during cycling, enabling higher active material loadings ($\geq$70−180 mg/cm^2), high energy density (approaching 70 Wh/kg), and facilitating ion transport through electrolyte that mitigates the solid state diffusion limitations that often arise with high active material loadings.[1,20,32,132,133]

VP 3D printing techniques, such as PμSL, DLP, and CLIP, expand the landscape for optimized geometries to overcome the increased ion transport lengths associated with thick, 3D electrodes. For example, Reale Batista et al. used simulation-driven geometry design to optimize topology of supercapacitor electrodes for energy density via PμSL and pyrolysis at 1000 °C in N_2 of PR48 and custom GO-containing TMPTA.[19] Alternatively, Katsuyama et al. printed supercapacitor electrodes with hierarchical porosity from Elegoo using SLA followed by pyrolysis at 1000 °C under vacuum and CO_2 that they coated in MnO_2 and incorporated into an asymmetric cell demonstrating a wide potential window of 1.8 V in $NaSO_4$.[37] A similar approach was taken by Rezaei et al. to produce SLA printed 3D pyrolytic carbon/Mn_3O_4 hybrid supercapacitor electrodes that demonstrated a gravimetric capacitance of 186 F/g with 92% capacitance retention after 5000 cycles.[106]

3D printed pyrolytic carbon can also serve as anodes in Li$^+$- and Na$^+$-batteries.[32,134] Commercial LIB anodes are typically fabricated via slurry casting of graphite with binders, which is limited by low electrical conductivity of the binder and tortuous ion diffusion pathways between active materials and binders.[1,127,135] In contrast, a monolithic 3D architected carbon electrode removes these factors, and 3D printing can enable uniform porosity and current distribution, which can aid in alleviating dendrite formation arising from locally high potentials and Li$^+$ concentrations.[32] For example, Narita et al. produced carbon-based 3D Li-ion battery anodes via pyrolysis of PR48 at 1000 °C, printed using a DLP technique (Figure 6A).[32] Upon galvanostatic cycling, the initial charging process exhibited a Coulombic efficiency of 78%, which increased upon

subsequent cycles to >99%. The electrode displayed a 25% capacity retention after 500 cycles at a high current density of 100 mA/g and their electrodes withstood a uniaxial compressive stress of 27 MPa, indicating their viability to withstand packaging pressures during commercial cell fabrication.

5.2. Electrocatalysis

3D printed carbon structures have been used as substrates for electrocatalysis due to their high specific surface areas enabling increased loading capacity of catalyst active material similar to energy storage application standards.[136,137] Peng et al.[138] utilized 3D printed graphene electrodes with hierarchical porous structures integrated with NiFeP nanosheets for water splitting, which exhibited high flexural strength and surface areas enabling a voltage range of 1.58 V at 30 mA/cm and improved ion transport rates for electrocatalysis compared to nonarchitected systems. Kou et al.[139] utilized 3D printed Ni electrodes with periodic structures to suppress gas bubble coalescence, jamming, and trapping. These electrodes demonstrated high areal current density of 1000 mA/cm^2 compared to 79.5 mA/cm^2 for commercial 3D Ni foam at an overpotential of 245 mV. 3D printed carbon materials can also be valuable for CO_2 conversion to valuable products due to their controlled structural and electronic properties and high CO_2 affinity.[140]

5.3. Mechanical Applications

Pyrolytic carbon materials fabricated by 3D printing have also emerged as high-performance mechanical materials. A target goal is achieving compressive strength equal to or greater than the 4 GPa demonstrated by high strength carbon fibers.[31] Bauer et al. fabricated honeycomb carbon nanolattices using DLW-2PP and pyrolysis that exhibit high mechanical strength, up to 3 GPa.[12] Unit cell design plays a critical role in high strength 3D carbon lattice production. An important consideration for mitigating distortion during pyrolysis is whether the lattice structure experiences stretching-dominated or bending-dominated deformation, as defined by Deshpande et al.[141] Triangular cells are considered the most rigid and stretching-dominated unit cell type.[142] Stretching-dominated lattices exhibit greater modulus and initial yield strength than bending-dominated lattices with the same relative density. This causes stretching-dominated structures to be more ideal for structural applications and isotropic shrinkage during pyrolysis conversion due to struts maintaining tension in line with the lattice nodes during load bearing, whereas bending-dominated structures are more ideal for energy absorption as their nodes bend away from notes toward the cell edges, causing softening.[141] Additionally, closed cell configurations, such as shell or plate unit cells, can afford higher strength and stiffness compared to beam-based structures by enhancing the interconnectivity between unit cell, reducing structural entropy and increasing the storage of strain energy.[143] For example, Crook et al. 3D printed a closed cell cubic and octet nanolattice structure via DLW-2PP printing followed by carbonization at 900 °C that exhibited a compressive strength of 3 GPa at 0.792 g/cm^3 and stiffness of 21.6 GPa, a > 600% improvement over analogous octet beam-based lattices (Figure 6B).[10]

5.4. Biomedical Applications

3D carbon structures have been incorporated into micro- and nano- electromechanical systems for biomedical *in vitro*

applications, such as biosensing, dielectrophoretic[144] and cell-sorting or trapping[145−147] systems. 3D printed pyrolytic carbon structures are valuable for biomedical applications due to their biocompatibility in addition to their conductive nature, enabling incorporation into devices that are promising candidates for drug delivery[148] and biosensing for human-machine interfaces such as neural probes and health-monitoring implants.[149] For example, Mishra et al. 3D printed hollow carbon microneedles with SU-8 and pyrolyzed at 900 °C under inert conditions.[148] The carbon needles exhibited promising hardness, biocompatibility, and thermal and chemical stability, enabling penetration of mouse skin repeatedly without breakage. Moreover, 3D carbon structures have shown potential as scaffolds for tissue engineering for both neural[150] and musculoskeletal applications.[151] For example, Islam et al. fabricated 3D carbon architectures by SLA 3D printing epoxy polymer followed by pyrolysis at 900 °C in nitrogen.[151] The carbon microlattices exhibited an elastic modulus around 2.28 MPa, which is acceptable for use in human tissue repair applications. Furthermore, Fuhrer et al. utilized 3D pyrolytic carbon structures as platforms for culturing neural stem cells.[150] Their structures facilitated electrical stimulus to cells, allowing the observation of cell responses in a system that is compatible with magnetic resonance imaging.[150] Additionally, Hemanth et al. and Yang et al. (Figure 6C) both generated 3D carbon microelectrodes from SU-8 photoresist using two-photon lithography with electrochemical sensitivity that enabled neurochemical dopamine detection.[17,58]

These advancements underscore the potential of these 3D microelectrodes in applications like sensitive electrochemical sensing and bioelectrochemistry, benefiting from high surface area and efficient electron transfer properties.

6. COMBINING CLIP AND PYROLYSIS

The DLP method of continuous liquid interface production (CLIP) has established itself as a 3D printing industry standard due to its exceptional combination of rapid printing (linear speed up to 17 mm/min) and smooth surface finish.[2,53,55] CLIP technology exploits a unique approach involving a continuous liquid interface, known as the dead zone, created by oxygen, which serves as a polymerization inhibitor that prevents adhesion to the window as a printed part is cured.[53] Recent advancements in high-resolution CLIP have additionally demonstrated the ability to mass produce high-resolution objects and resolve voxels as small as 2× 2 μm^2 in the print plane with 1 μm unsupported thicknesses.[152] Integration with injection CLIP (iCLIP) has yielded microfluidics. iCLIP mitigates overcuring via injecting resin into void spaces during printing, enabling negative space microchannel diameters as small as 50 μm.[2,153,154] These advancements have positioned CLIP as an ideal candidate for manufacturing 3D polymer templates with complex geometries.

CLIP has not previously been used in combination with pyrolysis to generate conductive carbon lattice structures. Herein we demonstrate the viability of combining CLIP and pyrolysis by using a commercial resin found in prior pyrolysis literature, PR48.[32] Using a CLIP printer with 5.4 μm pixel size, 8 mm diameter PR48 octet lattice disks with 50 μm diameter struts and void fractions of 88% (based on 500 μm^3 unit cells) designed with nTopology software were generated (Figure 7A). These PR48 disks were pyrolyzed using a thermogravimetric analysis (TGA) furnace at 800 °C in N_2 with a 5 °C/
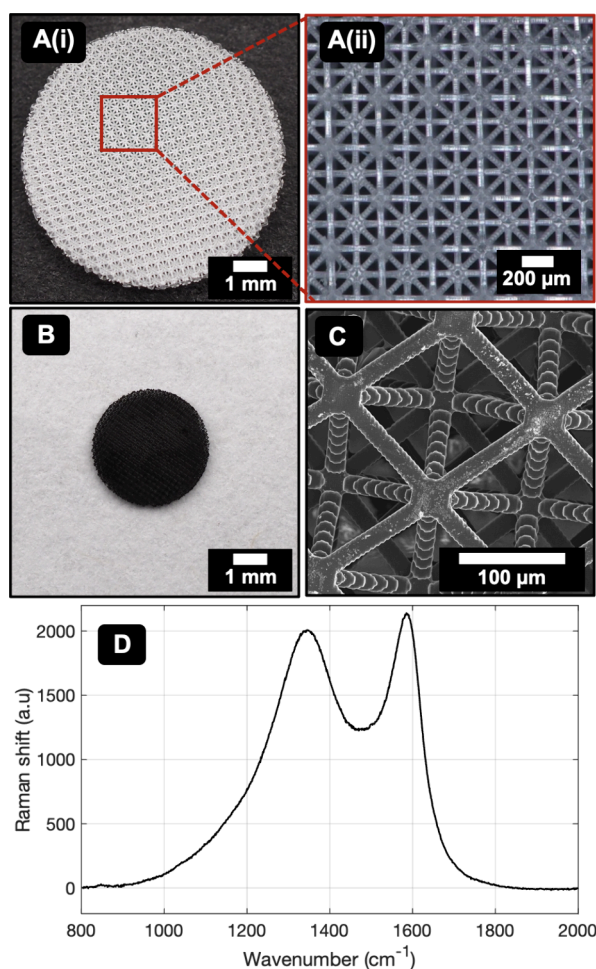
Figure 7. Optical images of a representative 8 mm diameter PR48 octet lattice disk with 50 μm diameter struts and 500 μm^3 unit cell (A) (i) after CLIP printing with (ii) inset showing the lattice pattern, and (B) after pyrolysis via a ramp in N_2 to 800 °C at 5 °C/min ramp rate; (C) scanning electron microscope image of a representative pyrolytic carbon lattice with 15 μm beams; (D) Raman data of 800 °C pyrolyzed PR48 lattice.

min ramp to achieve pyrolytic carbon lattice disks with 15 μm strut diameters (Figure 7B–C, Figure S1). The lattice features printed via CLIP remained intact and underwent approximately 65% linear shrinkage after conversion to carbon. Raman spectroscopy was conducted on a representative PR48 structure printed via CLIP and pyrolyzed at 800 °C. The PR48-derived carbon lattice structures demonstrated characteristic D and G bands of graphitic carbon with a I_{D1}/I_G ratio of 0.94 based on peak intensity after baseline subtraction (Figure 7D). See Supporting Information S1 for full experimental section.

To investigate the effect that heating treatment has on carbon structure output, lattice disk samples were subjected to a range of furnace conditions. Prior studies indicate that PR48 undergoes the bulk of its mass loss decomposition around 400 °C before arriving at complete carbonization at 650 °C.[32] Additionally, the highest char yield previously achieved using pure PR48 by Reale Batista et al. involved an hold at 300 °C in an oxidative environment.[19] Therefore, we investigated the impact of this condition and other conditions involving isothermal holds, including a hold in N_2 at 400 °C and holds in air at 300 and 260 °C all with 800 °C final pyrolysis

temperature and 5 °C/min ramp rates. The 800 °C pyrolysis run in N_2 with no holds was used as a control. Modifying the furnace procedure affected the surface morphology of the lattice beams, with the addition of the oxidative holds (Figure 8A–C) leading to increased surface texture topology compared
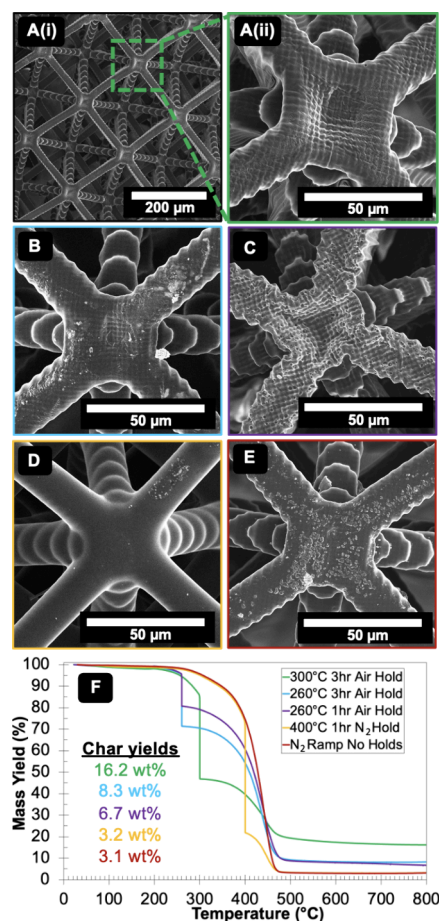

Figure 8. Scanning electron microscope images of PR48 octet lattices that were pyrolyzed at 800 °C in N_2 with different heat treatments, including (A) a 3 h air 300 °C hold with (i) image of several nodes and (ii) image of a single node, (B) 3 h air 260 °C hold, (C) 1 h air 260 °C hold, (D) 1 h N_2 400 °C hold, (E) control with no isothermal holds; (F) TGA curves displaying mass loss for each of these heat treatments with char yield being representative of the final mass yield at 800 °C.

to smoother samples produced in an inert atmosphere (Figure 8D,E). Additionally, the runs with longer isothermal holds in similar conditions lead to less surface deformities, for example adding a 1 h 400 °C hold (Figure 8D) yields smoother surface than the baseline N_2 ramp (Figure 8E) and holding at 260 °C in air (Figure 8B) versus 1 h (Figure 8C) causes fewer rough edges around the outside of the beams. Heat treatment also affected the char yield, with the control N_2 ramp run yielding 3.1 wt % char yield while the greatest char yield of 16.2 wt % was achieved via the procedure with a 3-h isothermal hold at 300 °C in air (Figure 8F, Tables 1 and 4). We hypothesize that different heat treatments result in different surface topographies and char yields by affecting the rate and pathway of off-gassing pyrolysis byproducts and the degree of carbon graphitization. Conducting isothermal holds around temperatures where rapid mass loss occurs may enable volatiles to escape more gradually through available pathways in the

polymer template while the polymer structures rearrange. Additionally, it has been shown that an oxidative treatment before inert pyrolysis causes dehydrogenation, aromatization, and oxidation of the polymer functional groups that help stabilize the polymer structure before cyclization and graphitization in inert gas at higher temperatures.[87]

Further investigation into pyrolysis of 3D printed polymers could advance understanding of this process by using an evolved gas analysis technique, such as mass spectrometry, to observe of the type, rate, and residence time of volatile gases produced at different temperatures.[155] Future studies should also prioritize conducting (electro)chemical and mechanical characterization on samples pyrolyzed under different pyrolysis conditions to connect processing conditions to properties like electrochemically active surface area, electrical resistance, strength, degree of graphitization, and resulting surface topography. One important consideration for sample mechanical integrity is that samples can be handled and assembled into electrochemical cells systems without breaking or cracking, which requires compressive strength on the order of 100 kPa or higher.[34,83] Mitigating material loss by achieving higher char yields is also desirable to produce larger objects.

This work demonstrates the viability of combining CLIP and pyrolysis for production of well-defined 3D carbon structures with high surface area features for energy storage. The 15 μm lattice feature sizes are, to the best of our knowledge, the highest resolution pyrolytic carbon achieved via a DLP-based printing technology. Future work should aim toward development of tailored custom resins designed for printability via CLIP and refinement of the pyrolysis process to achieve graphitic carbon structures that experience high mechanical strength with feature dimensions of 5−7 μm, the width of carbon fibers.[31,156]

7. CONCLUSION

Herein we have reviewed the existing literature on pyrolysis of 3D printed polymers to carbon structures. One significant shortcoming of existing work is that the commercial resins often used in these studies, such as acrylate-based PR48 and epoxy-based SU-8, were not originally designed for pyrolysis[17,32,74] and therefore inherently are not tailored for the most optimal pyrolysis char yield output. Several custom polymer resins have been developed to be more intentional about the molecular composition of the pyrolysis precursor structure, for example by incorporating carbon-containing additives into acrylate-based monomers and generating aromatic polyimide structures.[52,82] Among the custom resin compositions, the structures with aryl cyclic functional groups and nitrile-containing groups that cyclize easily demonstrate the most promise in terms of high char yield and structural integrity and should be investigated further. Most often, acrylate groups are incorporated into these resins to enable radical polymerization during 3D printing. Additives such as graphene oxide also show promise for enhancing porosity and conductivity. Regarding the furnace conditions used to pyrolyze these materials, reaching temperatures greater than 900−1000 °C while heating in inert environments after stabilization steps in oxygen most often facilitates production of carbon with useful structural and electrochemical properties.

While several tailored custom resin systems developed to date are promising, they still often fall short when compared to the electrical conductivity (>100 S/m) and structural integrity (mechanical strength ≥4 GPa) of industry standard carbon fiber precursors that are used outside of the 3D-printing field.[31,157] Therefore, future studies must improve upon existing 3D printing resin compositions to generate graphitic carbon structures that have electrochemical characteristics conducive for applications in energy materials. Researchers should take direct inspiration from the polymers typically used in carbon fiber production, for example polyacrylonitrile, and should aim to advance scalable 3D printing procedures to achieve features like lattice beam diameters on the scale of carbon fiber precursor diameters, which are approximately 5−7 μm.[156] Focusing on light-based 3D printing methods that demonstrate both the speed and resolution capabilities for microfabrication of energy materials at industry scale is recommended. For example, in this work we report the fabrication of pyrolytic carbon structures with 15 μm beams with CLIP; to our knowledge, these are the smallest lattice features produced via a digital light projection-based 3D printing method. It is also necessary to further understand the carbonization process of 3D printed polymer during pyrolysis, which can be accomplished via by establishing new *in situ* characterization capabilities inside furnace systems to monitor degradation processes real time. Further investigation into incorporating catalytic graphitization into the pyrolysis process is also recommended due to the opportunity to more effectively volatilize noncarbon elements in the 3D printed precursor structure and mitigate the high energy usage caused by heating at temperatures greater than 1000 °C.

Embracing the fusion of 3D printing and pyrolysis toward development of groundbreaking carbon structures not only opens new horizons for sustainable energy storage solutions but also marks our collective stride toward an innovative and environmentally conscious future. This endeavor supports the mitigation of fossil fuel usage and facilitates the incorporation of electrification and renewable technologies to redefine society's current energy landscape.

■ ASSOCIATED CONTENT

ⓢ Supporting Information

The Supporting Information is available free of charge at https://pubs.acs.org/doi/10.1021/jacsau.4c00555.

> Detailed experimental section for fabrication, pyrolysis, and characterization of the carbon lattice disks generated for Section 6; lower magnification scanning electron microscope image of the pyrolytic carbon lattice sample included in Figure 7C (PDF)

■ AUTHOR INFORMATION

Corresponding Authors

Max A. Saccone − *Department of Chemical Engineering, Stanford University, Stanford, California 94305, United States; Department of Radiology, Stanford University, Stanford, California 94305, United States; Department of Mechanical Engineering, University of Colorado Boulder, Boulder, Colorado 80309, United States;* ⓞ orcid.org/0000-0003-3846-2908; Email: max.saccone@colorado.edu

Jennifer Q. Lu − *Department of Materials Science & Engineering, University of California, Merced, Merced, California 95343, United States;* ⓞ orcid.org/0000-0002-1716-0380; Email: jlu5@ucmerced.edu

Joseph M. DeSimone − *Department of Chemical Engineering, Stanford University, Stanford, California 94305, United States; Department of Radiology, Stanford University,*

Stanford, California 94305, United States; ● orcid.org/0000-0001-9521-5095; Email: jmdesimone@stanford.edu

Authors

Philip R. Onffroy − *Department of Chemical Engineering, Stanford University, Stanford, California 94305, United States;* ● orcid.org/0000-0003-1537-5174

Samuel Chiovoloni − *Department of Materials Science & Engineering, University of California, Merced, Merced, California 95343, United States*

Han Lin Kuo − *Department of Materials Science & Engineering, University of California, Merced, Merced, California 95343, United States*

Complete contact information is available at:
https://pubs.acs.org/10.1021/jacsau.4c00555

Author Contributions

¶P.R.O. and S.C. contributed equally to this work. CRediT: **Philip R. Onffroy** conceptualization, data curation, methodology, project administration, validation, visualization, writing - original draft, writing - review & editing; **Samuel Chiovoloni** conceptualization, data curation, methodology, visualization, writing - original draft, writing - review & editing; **Han-Lin Kuo** conceptualization, data curation, methodology, visualization, writing - original draft, writing - review & editing; **Max A. Saccone** conceptualization, data curation, investigation, methodology, supervision, validation, writing - review & editing; **Jennifer Q. Lu** conceptualization, funding acquisition, investigation, project administration, resources, supervision, writing - review & editing; **Joseph M. DeSimone** conceptualization, funding acquisition, investigation, project administration, resources, supervision, writing - review & editing.

Notes

The authors declare the following competing financial interest(s): Joseph M. DeSimone reports financial support to the DeSimone research group was provided by startup funds from Stanford University School of Medicine and the School of Engineering. Philip R. Onffroy reports financial support was provided by the Knight-Hennessy Scholarship and National Science Foundation (NSF) Graduate Research Fellowship Program Grant #DGE-2146755. Jennifer Q. Lu reports financial support to the Lu research group was provided by National Aeronautics and Space Administration (NASA) Grant #NNH18ZHA008CMIROG6R and NSF Grant #CHE-1900647. Joseph M DeSimone was a cofounder of, and has financial stake in, Carbon, Inc., a CLIP-based 3D printing company. Joseph M DeSimone declares that he is an inventor on related US Patent 9,040,090, U.S. Patent 9,216,546, U.S. Patent 9,360,757, and others. Joseph M DeSimone declares that as a co-founder, board member, and former CEO of Carbon, Inc., and as an active researcher in additive manufacturing, that he has had hundreds of social media and journalist interviews about Carbon and additive manufacturing. Max A. Saccone advises 3D Architech, a VP-based metal 3D printing company. The authors declare that they have no other competing interests.

■ REFERENCES

(1) Chandrasekaran, S.; Lin, D.; Li, Y.; Worsley, M. A. Aerogels, Additive Manufacturing, and Energy Storage. *Joule* **2023**, *7* (5), 866−883.

(2) Hsiao, K.; Lee, B. J.; Samuelsen, T.; Lipkowitz, G.; Kronenfeld, J. M.; Ilyn, D.; Shih, A.; Dulay, M. T.; Tate, L.; Shaqfeh, E. S. G.; DeSimone, J. M. Single-Digit-Micrometer-Resolution Continuous Liquid Interface Production. *Sci. Adv.* **2022**, *8* (46), No. eabq2846.

(3) Vidler, C.; Crozier, K.; Collins, D. Ultra-Resolution Scalable Microprinting. *Microsyst. Nanoeng.* **2023**, *9* (1), 67.

(4) Sun, C.; Wang, Y.; McMurtrey, M. D.; Jerred, N. D.; Liou, F.; Li, J. Additive Manufacturing for Energy: A Review. *Appl. Energy* **2021**, *282*, 116041.

(5) Chaudhary, R.; Fabbri, P.; Leoni, E.; Mazzanti, F.; Akbari, R.; Antonini, C. Additive Manufacturing by Digital Light Processing: A Review. *Prog. Addit. Manuf.* **2023**, *8* (2), 331−351.

(6) Blyweert, P.; Nicolas, V.; Fierro, V.; Celzard, A. 3D Printing of Carbon-Based Materials: A Review. *Carbon* **2021**, *183*, 449−485.

(7) Han, J.; Johnson, I.; Chen, M. 3D Continuously Porous Graphene for Energy Applications. *Adv. Mater.* **2022**, *34* (15), 2108750.

(8) Staggs, J. E. J. A Simple Model of Polymer Pyrolysis Including Transport of Volatiles. *Fire Saf. J.* **2000**, *34* (1), 69−80.

(9) Eggeler, Y. M.; Chan, K. C.; Sun, Q.; Lantada, A. D.; Mager, D.; Schwaiger, R.; Gumbsch, P.; Schröder, R.; Wenzel, W.; Korvink, J. G.; Islam, M. A Review on 3D Architected Pyrolytic Carbon Produced by Additive Micro/Nanomanufacturing. *Adv. Funct. Mater.* **2024**, *34*, 2302068.

(10) Crook, C.; Bauer, J.; Guell Izard, A.; Santos de Oliveira, C.; Martins de Souza e Silva, J.; Berger, J. B.; Valdevit, L. Plate-Nanolattices at the Theoretical Limit of Stiffness and Strength. *Nat. Commun.* **2020**, *11* (1), 1579.

(11) Al-Ketan, O.; Rowshan, R.; Abu Al-Rub, R. K. Topology-Mechanical Property Relationship of 3D Printed Strut, Skeletal, and Sheet Based Periodic Metallic Cellular Materials. *Addit. Manuf.* **2018**, *19*, 167−183.

(12) Bauer, J.; Schroer, A.; Schwaiger, R.; Kraft, O. Approaching Theoretical Strength in Glassy Carbon Nanolattices. *Nat. Mater.* **2016**, *15* (4), 438−443.

(13) Kudo, A.; Bosi, F. Nanographitic Coating Enables Hydrophobicity in Lightweight and Strong Microarchitected Carbon. *Commun. Mater.* **2020**, *1* (1), 1−10.

(14) Kou, T.; Wang, S.; Shi, R.; Zhang, T.; Chiovoloni, S.; Lu, J. Q.; Chen, W.; Worsley, M. A.; Wood, B. C.; Baker, S. E.; Duoss, E. B.; Wu, R.; Zhu, C.; Li, Y. Periodic Porous 3D Electrodes Mitigate Gas Bubble Traffic during Alkaline Water Electrolysis at High Current Densities. *Adv. Energy Mater.* **2020**, *10* (46), 2002955.

(15) Bian, B.; Shi, D.; Cai, X.; Hu, M.; Guo, Q.; Zhang, C.; Wang, Q.; Sun, A. X.; Yang, J. 3D Printed Porous Carbon Anode for Enhanced Power Generation in Microbial Fuel Cell. *Nano Energy* **2018**, *44*, 174−180.

(16) Kassegne, S.; Vomero, M.; Gavuglio, R.; Hirabayashi, M.; Özyilmaz, E.; Nguyen, S.; Rodriguez, J.; Özyilmaz, E.; Van Niekerk, P.; Khosla, A. Electrical Impedance, Electrochemistry, Mechanical Stiffness, and Hardness Tunability in Glassy Carbon MEMS μECoG Electrodes. *Microelectron. Eng.* **2015**, *133*, 36−44.

(17) Hemanth, S.; Caviglia, C.; Keller, S. S. Suspended 3D Pyrolytic Carbon Microelectrodes for Electrochemistry. *Carbon* **2017**, *121*, 226−234.

(18) Yao, B.; Peng, H.; Zhang, H.; Kang, J.; Zhu, C.; Delgado, G.; Byrne, D.; Faulkner, S.; Freyman, M.; Lu, X.; Worsley, M. A.; Lu, J.

Q.; Li, Y. Printing Porous Carbon Aerogels for Low Temperature Supercapacitors. *Nano Lett.* **2021**, *21* (9), 3731−3737.

(19) Reale Batista, M. D.; Chandrasekaran, S.; Moran, B. D.; Salazar de Troya, M.; Pinongcos, A.; Wang, Z.; Hensleigh, R.; Carleton, A.; Zeng, M.; Roy, T.; Lin, D.; Xue, X.; Beck, V. A.; Tortorelli, D. A.; Stadermann, M.; Zheng, R.; Li, Y.; Worsley, M. A. Design and Additive Manufacturing of Optimized Electrodes for Energy Storage Applications. *Carbon* **2023**, *205*, 262−269.

(20) Lin, D.; Chandrasekaran, S.; Forien, J.-B.; Xue, X.; Pinongcos, A.; Coester, E.; Worsley, M. A.; Li, Y. 3D-Printed Graded Electrode with Ultrahigh MnO2 Loading for Non-Aqueous Electrochemical Energy Storage. *Adv. Energy Mater.* **2023**, *13* (20), 2300408.

(21) Boretti, A.; Castelletto, S. A Perspective on 3D Printing of Silicon Carbide. *J. Eur. Ceram. Soc.* **2024**, *44* (3), 1351−1360.

(22) Chen, Z.; Li, Z.; Li, J.; Liu, C.; Lao, C.; Fu, Y.; Liu, C.; Li, Y.; Wang, P.; He, Y. 3D Printing of Ceramics: A Review. *J. Eur. Ceram. Soc.* **2019**, *39* (4), 661−687.

(23) Han, J.; Liu, C.; Bradford-Vialva, R. L.; Klosterman, D. A.; Cao, L. Additive Manufacturing of Advanced Ceramics Using Preceramic Polymers. *Materials* **2023**, *16* (13), 4636.

(24) Du, J.; Fu, G.; Xu, X.; Elshahawy, A. M.; Guan, C. 3D Printed Graphene-Based Metamaterials: Guesting Multi-Functionality in One Gain. *Small* **2023**, *19* (19), 2207833.

(25) Fu, K.; Yao, Y.; Dai, J.; Hu, L. Progress in 3D Printing of Carbon Materials for Energy-Related Applications. *Adv. Mater.* **2017**, *29* (9), 1603486.

(26) Guo, H.; Lv, R.; Bai, S. Recent Advances on 3D Printing Graphene-Based Composites. *Nano Mater. Sci.* **2019**, *1* (2), 101−115.

(27) Schwarcz, J. *Charcoal is one of the most important substances ever discovered*; Office for Science and Society. https://www.mcgill.ca/oss/article/environment-health/charcoal-one-most-important-substances-ever-discovered (accessed 2024−05−21).

(28) Edison, T. A. Electric Lamp. US223898A, January 27, 1880. https://patents.google.com/patent/US223898A/en (accessed 2024−03−16).

(29) Park, S.-J. *Carbon Fibers*; Springer Series in Materials Science; Springer: Singapore, 2018; Vol. 210. DOI: 10.1007/978-981-13-0538-2.

(30) Gorss, J. *High Performance Carbon Fibers*; American Chemical Society, 2003; pp 1−4.

(31) Huang, X. Fabrication and Properties of Carbon Fibers. *Materials* **2009**, *2* (4), 2369−2403.

(32) Narita, K.; Citrin, M. A.; Yang, H.; Xia, X.; Greer, J. R. 3D Architected Carbon Electrodes for Energy Storage. *Adv. Energy Mater.* **2021**, *11* (5), 2002637.

(33) Chyr, G.; DeSimone, J. M. Review of High-Performance Sustainable Polymers in Additive Manufacturing. *Green Chem.* **2023**, *25* (2), 453−466.

(34) Steldinger, H.; Esposito, A.; Brunnengräber, K.; Gläsel, J.; Etzold, B. J. M. Activated Carbon in the Third Dimension—3D Printing of a Tuned Porous Carbon. *Adv. Sci.* **2019**, *6* (19), 1901340.

(35) Szczurek, A.; Ortona, A.; Ferrari, L.; Rezaei, E.; Medjahdi, G.; Fierro, V.; Bychanok, D.; Kuzhir, P.; Celzard, A. Carbon Periodic Cellular Architectures. *Carbon* **2015**, *88*, 70−85.

(36) Sun, Q.; Dolle, C.; Kurpiers, C.; Kraft, K.; Islam, M.; Schwaiger, R.; Gumbsch, P.; Eggeler, Y. M. In Situ Pyrolysis of 3D Printed Building Blocks for Functional Nanoscale Metamaterials. *Adv. Funct. Mater.* **2024**, *34*, 2302358.

(37) Katsuyama, Y.; Haba, N.; Kobayashi, H.; Iwase, K.; Kudo, A.; Honma, I.; Kaner, R. B. Macro- and Nano-Porous 3D-Hierarchical Carbon Lattices for Extraordinarily High Capacitance Supercapacitors. *Adv. Funct. Mater.* **2022**, *32* (24), 2201544.

(38) Zakhurdaeva, A.; Dietrich, P.-I.; Hölscher, H.; Koos, C.; Korvink, J.; Sharma, S. Custom-Designed Glassy Carbon Tips for Atomic Force Microscopy. *Micromachines* **2017**, *8* (9), 285.

(39) Blyweert, P.; Nicolas, V.; Macutkevic, J.; Fierro, V.; Celzard, A. Tannin-Based Resins for 3D Printing of Porous Carbon Architectures. *ACS Sustain. Chem. Eng.* **2022**, *10* (23), 7702−7711.

(40) Blyweert, P.; Nicolas, V.; Fierro, V.; Celzard, A. 3D-Printed Carbons with Improved Properties and Oxidation Resistance. *ACS Sustain. Chem. Eng.* **2023**, *11* (21), 8055−8064.

(41) Lewis, J. A. Direct Ink Writing of 3D Functional Materials. *Adv. Funct. Mater.* **2006**, *16* (17), 2193−2204.

(42) Tetik, H.; Wang, Y.; Sun, X.; Cao, D.; Shah, N.; Zhu, H.; Qian, F.; Lin, D. Additive Manufacturing of 3D Aerogels and Porous Scaffolds: A Review. *Adv. Funct. Mater.* **2021**, *31* (45), 2103410.

(43) Usselmann, M.; Bansmann, J.; Kuehne, A. J. C. Switchable Polyacrylonitrile-Copolymer for Melt-Processing and Thermal Carbonization—3D Printing of Carbon Supercapacitor Electrodes with High Capacitance. *Adv. Mater.* **2023**, *35* (6), 2208484.

(44) Shao, Y.; Guizani, C.; Grosseau, P.; Chaussy, D.; Beneventi, D. Use of Lignocellulosic Materials and 3D Printing for the Development of Structured Monolithic Carbon Materials. *Compos. Part B Eng.* **2018**, *149*, 206−215.

(45) Yao, B.; Chandrasekaran, S.; Zhang, J.; Xiao, W.; Qian, F.; Zhu, C.; Duoss, E. B.; Spadaccini, C. M.; Worsley, M. A.; Li, Y. Efficient 3D Printed Pseudocapacitive Electrodes with Ultrahigh MnO2 Loading. *Joule* **2019**, *3* (2), 459−470.

(46) Zhou, G.; Li, M.; Liu, C.; Liu, C.; Li, Z.; Mei, C. 3D Printed Nitrogen-Doped Thick Carbon Architectures for Supercapacitor: Ink Rheology and Electrochemical Performance. *Adv. Sci.* **2023**, *10* (10), 2206320.

(47) Gratson, G. M.; Lewis, J. A. Phase Behavior and Rheological Properties of Polyelectrolyte Inks for Direct-Write Assembly. *Langmuir* **2005**, *21* (1), 457−464.

(48) Jabari, E.; Toyserkani, E. Micro-Scale Aerosol-Jet Printing of Graphene Interconnects. *Carbon* **2015**, *91*, 321−329.

(49) Mao, A.; Mitsuboshi, H.; Trochon, M.; Zhang, X.; Trinh, L.; Keynia, S.; Fan, P.; Kraiem, N.; Huang, X.; Li, N.; Li, P.; Wu, Z.; Sun, W.; Cui, B.; Silvain, J.-F.; Hara, M.; Yoshimura, M.; Marshall, K. L.; Anthamatten, M.; Lu, Y. Evolution of Chemical and Mechanical Properties in Two-Photon Polymerized Materials during Pyrolysis. *Carbon* **2023**, *208*, 384−389.

(50) Whyte, D. J.; Doeven, E. H.; Sutti, A.; Kouzani, A. Z.; Adams, S. D. Volumetric Additive Manufacturing: A New Frontier in Layer-Less 3D Printing. *Addit. Manuf.* **2024**, *84*, 104094.

(51) Regehly, M.; Garmshausen, Y.; Reuter, M.; König, N. F.; Israel, E.; Kelly, D. P.; Chou, C.-Y.; Koch, K.; Asfari, B.; Hecht, S. Xolography for Linear Volumetric 3D Printing. *Nature* **2020**, *588* (7839), 620−624.

(52) Hensleigh, R. M.; Cui, H.; Oakdale, J. S.; Ye, J. C.; Campbell, P. G.; Duoss, E. B.; Spadaccini, C. M.; Zheng, X.; Worsley, M. A. Additive Manufacturing of Complex Micro-Architected Graphene Aerogels. *Mater. Horiz.* **2018**, *5* (6), 1035−1041.

(53) Tumbleston, J. R.; Shirvanyants, D.; Ermoshkin, N.; Janusziewicz, R.; Johnson, A. R.; Kelly, D.; Chen, K.; Pinschmidt, R.; Rolland, J. P.; Ermoshkin, A.; Samulski, E. T.; DeSimone, J. M. Continuous Liquid Interface Production of 3D Objects. *Science* **2015**, *347* (6228), 1349−1352.

(54) Pagac, M.; Hajnys, J.; Ma, Q.-P.; Jancar, L.; Jansa, J.; Stefek, P.; Mesicek, J. A Review of Vat Photopolymerization Technology: Materials, Applications, Challenges, and Future Trends of 3D Printing. *Polymers* **2021**, *13* (4), 598.

(55) Bagheri, A.; Jin, J. Photopolymerization in 3D Printing. *ACS Appl. Polym. Mater.* **2019**, *1* (4), 593−611.

(56) Marques, C. A.; Rhodes, L. C.; Benedičič, I.; Naritsuka, M.; Naden, A. B.; Li, Z.; Komarek, A. C.; Mackenzie, A. P.; Wahl, P. Atomic-Scale Imaging of Emergent Order at a Magnetic Field-Induced Lifshitz Transition. *Sci. Adv.* **2022**, *8* (39), No. eabo7757.

(57) Hahn, V.; Kiefer, P.; Frenzel, T.; Qu, J.; Blasco, E.; Barner-Kowollik, C.; Wegener, M. Rapid Assembly of Small Materials Building Blocks (Voxels) into Large Functional 3D Metamaterials. *Adv. Funct. Mater.* **2020**, *30* (26), 1907795.

(58) Yang, C.; Cao, Q.; Puthongkham, P.; Lee, S. T.; Ganesana, M.; Lavrik, N. V.; Venton, B. J. 3D-Printed Carbon Electrodes for Neurotransmitter Detection. *Angew. Chem., Int. Ed.* **2018**, *57* (43), 14255−14259.

(59) Comroe, M. L.; Kolasinski, K. W.; Saha, D. Direct Ink 3D Printing of Porous Carbon Monoliths for Gas Separations. *Molecules* **2022**, *27* (17), 5653.

(60) Catarineu, N. R.; Lin, D.; Zhu, C.; Oyarzun, D. I.; Li, Y. High-Performance Aqueous Zinc-Ion Hybrid Capacitors Based on 3D Printed Metal-Organic Framework Cathodes. *Chem. Eng. J.* **2023**, *465*, 142544.

(61) Jonusauskas, L.; Gailevičius, D.; Mikoliūnaitė, L.; Sakalauskas, D.; Šakirzanovas, S.; Juodkazis, S.; Malinauskas, M. Optically Clear and Resilient Free-Form µ-Optics 3D-Printed via Ultrafast Laser Lithography. *Materials* **2017**, *10* (1), 12.

(62) Liu, J.; Liu, Y.; Deng, C.; Yu, K.; Fan, X.; Zhang, W.; Tao, Y.; Hu, H.; Deng, L.; Xiong, W. 3D Printing Nano-Architected Semiconductors Based on Versatile and Customizable Metal-Bound Composite Photoresins. *Adv. Mater. Technol.* **2022**, *7* (6), 2101230.

(63) Gunderson, C.; Rohbeck, N.; Tranchant, M.; Michler, J.; Philippe, L. Nanoscale 3D Electroforming by Template Pyrolysis. *Adv. Eng. Mater.* **2021**, *23* (5), 2001293.

(64) Desponds, A.; Banyasz, A.; Chateau, D.; Tellal, A.; Venier, A.; Meille, S.; Montagnac, G.; Chevalier, J.; Andraud, C.; Baldeck, P. L.; Parola, S. 3D Printing and Pyrolysis of Optical ZrO2 Nanostructures by Two-Photon Lithography: Reduced Shrinkage and Crystallization Mediated by Nanoparticles Seeds. *Small* **2021**, *17* (42), 2102486.

(65) Sun, Q.; Dolle, C.; Kurpiers, C.; Schwaiger, R.; Gumbsch, P.; Eggeler, Y. M. In Situ Pyrolysis of 3D Printed Microstructures - an ESEM Study. *Microsc. Microanal.* **2022**, *28* (S1), 2346−2348.

(66) Pan, J. Y.; Rezaei, B.; Anhøj, T. A.; Larsen, N. B.; Keller, S. S. Hybrid Microfabrication of 3D Pyrolytic Carbon Electrodes by Photolithography and Additive Manufacturing. *Micro Nano Eng.* **2022**, *15*, 100124.

(67) Natu, R.; Islam, M.; Martinez-Duarte, R. Shrinkage Analysis of Carbon Micro Structures Derived from SU-8 Photoresist. *ECS Trans.* **2016**, *72* (1), 27.

(68) Taale, M.; Schamberger, B.; Monclus, M. A.; Dolle, C.; Taheri, F.; Mager, D.; Eggeler, Y. M.; Korvink, J. G.; Molina-Aldareguia, J. M.; Selhuber-Unkel, C.; Lantada, A. D.; Islam, M. Microarchitected Compliant Scaffolds of Pyrolytic Carbon for 3D Muscle Cell Growth. *Adv. Healthc. Mater.* **2024**, *13* (9), 2303485.

(69) Korhonen, H.; Sinh, L. H.; Luong, N. D.; Lehtinen, P.; Verho, T.; Partanen, J.; Seppälä, J. Fabrication of Graphene-Based 3D Structures by Stereolithography. *Phys. Status Solidi A* **2016**, *213* (4), 982−985.

(70) Cherevko, A. I.; Nikovskiy, I. A.; Nelyubina, Y. V.; Skupov, K. M.; Efimov, N. N.; Novikov, V. V. 3D-Printed Porous Magnetic Carbon Materials Derived from Metal-Organic Frameworks. *Polymers* **2021**, *13* (22), 3881.

(71) Tian, P.; Chen, C.; Hu, J.; Qi, J.; Wang, Q.; Chen, J. C.-M.; Cavanaugh, J.; Peng, Y.; Cheng, M. M.-C. A Novel Fabrication Method of Carbon Electrodes Using 3D Printing and Chemical Modification Process. *Biomed. Microdevices* **2018**, *20* (1), 4.

(72) Blyweert, P.; Nicolas, V.; Fierro, V.; Celzard, A. Experimental Design Optimization of Acrylate—Tannin Photocurable Resins for 3D Printing of Bio-Based Porous Carbon Architectures. *Molecules* **2022**, *27* (7), 2091.

(73) Niblett, D.; Guo, Z.; Holmes, S.; Niasar, V.; Prosser, R. Utilization of 3D Printed Carbon Gas Diffusion Layers in Polymer Electrolyte Membrane Fuel Cells. *Int. J. Hydrog. Energy* **2022**, *47* (55), 23393−23410.

(74) Kudo, A.; Kanamaru, K.; Han, J.; Tang, R.; Kisu, K.; Yoshii, T.; Orimo, S.; Nishihara, H.; Chen, M. Stereolithography 3D Printed Carbon Microlattices with Hierarchical Porosity for Structural and Functional Applications. *Small* **2023**, *19*, 2301525.

(75) Katsuyama, Y.; Kudo, A.; Kobayashi, H.; Han, J.; Chen, M.; Honma, I.; Kaner, R. B. A 3D-Printed, Freestanding Carbon Lattice for Sodium Ion Batteries. *Small* **2022**, *18* (29), 2202277.

(76) Kudo, A.; Misseroni, D.; Wei, Y.; Bosi, F. Compressive Response of Non-Slender Octet Carbon Microlattices. *Front. Mater.* **2019**, *6*, 169.

(77) Park, S. H.; Kaur, M.; Yun, D.; Kim, W. S. Hierarchically Designed Electron Paths in 3D Printed Energy Storage Devices. *Langmuir* **2018**, *34* (37), 10897−10904.

(78) Lédé, J. Cellulose Pyrolysis Kinetics: An Historical Review on the Existence and Role of Intermediate Active Cellulose. *J. Anal. Appl. Pyrolysis* **2012**, *94*, 17−32.

(79) Perepelkin, K. E. Carbon Fibres with Specific Physical and Physicochemical Properties Based on Hydrated Cellulose and Polyacrylonitrile Precursors. A Review. *Fibre Chem.* **2002**, *34* (4), 271−280.

(80) Günaydin, H.; Salman, S.; Tüzün, N. Ş.; Avci, D.; Aviyente, V. Modeling the Free Radical Polymerization of Acrylates. *Int. J. Quantum Chem.* **2005**, *103* (2), 176−189.

(81) Rezaei, B.; Pan, J. Y.; Gundlach, C.; Keller, S. S. Highly Structured 3D Pyrolytic Carbon Electrodes Derived from Additive Manufacturing Technology. *Mater. Des.* **2020**, *193*, 108834.

(82) Arrington, C. B.; Rau, D. A.; Vandenbrande, J. A.; Hegde, M.; Williams, C. B.; Long, T. E. 3D Printing Carbonaceous Objects from Polyimide Pyrolysis. *ACS Macro Lett.* **2021**, *10* (4), 412−418.

(83) Lu, Y.; Hu, J.; Ng, K. W. J.; Hu, X. Micro-Fabrication of Glassy Carbon with Low Shrinkage and High Char Yield Using High-Performance Photocurable Phthalonitrile (PN) Resins. *Addit. Manuf.* **2024**, *83*, 104053.

(84) Bobrin, V. A.; Hackbarth, H. G.; Yao, Y.; Kundu, D.; Bedford, N. M.; Kuchel, R. P.; Zhang, J.; Corrigan, N.; Boyer, C. Design and 3D Printing of Polyacrylonitrile-Derived Nanostructured Carbon Architectures. *Small Sci.* **2024**, *4* (4), 2300275.

(85) Idrees, M.; Ahmed, S.; Mohammed, Z.; Korivi, N. S.; Rangari, V. 3D Printed Supercapacitor Using Porous Carbon Derived from Packaging Waste. *Addit. Manuf.* **2020**, *36*, 101525.

(86) Inagaki, M.; Ohta, N.; Hishiyama, Y. Aromatic Polyimides as Carbon Precursors. *Carbon* **2013**, *61*, 1−21.

(87) Rahaman, M. S. A.; Ismail, A. F.; Mustafa, A. A Review of Heat Treatment on Polyacrylonitrile Fiber. *Polym. Degrad. Stab.* **2007**, *92* (8), 1421−1432.

(88) Park, S.; Tian, R.; Coelho, J.; Nicolosi, V.; Coleman, J. N. Quantifying the Trade-Off between Absolute Capacity and Rate Performance in Battery Electrodes. *Adv. Energy Mater.* **2019**, *9* (33), 1901359.

(89) Fu, Z.; Liu, B.; Liu, Y.; Li, B.; Zhang, H. Detailed Cyclization Pathways Identification of Polyacrylonitrile and Poly(Acrylonitrile-Co-Itaconic Acid) by in Situ FTIR and Two-Dimensional Correlation Analysis. *Ind. Eng. Chem. Res.* **2018**, *57* (24), 8348−8359.

(90) Chazot, C. A. C.; Creighton, M. A.; Hart, A. J. Interfacial Photopolymerization: A Method for Light-Based Printing of Thermo-plastics. *ACS Appl. Mater. Interfaces* **2023**, *15* (25), 31009−31019.

(91) Bobrin, V. A.; Hackbarth, H. G.; Bonsu, J. O.; Yao, Y.; Bedford, N. M.; Kundu, D.; Zhang, J.; Corrigan, N.; Boyer, C. Microphase Separation 3D Printing of Binary Inorganic Polymer Precursors to Prepare Nanostructured Carbon-Ceramic Multimaterials. *Adv. Mater. Technol.* **2024**, *9* (13), 2400337.

(92) Blazsó, M. Recent Trends in Analytical and Applied Pyrolysis of Polymers. *J. Anal. Appl. Pyrolysis* **1997**, *39* (1), 1−25.

(93) Liu, Y.; Wang, H.; Ho, J.; Ng, R. C.; Ng, R. J. H.; Hall-Chen, V. H.; Koay, E. H. H.; Dong, Z.; Liu, H.; Qiu, C.-W.; Greer, J. R.; Yang, J. K. W. Structural Color Three-Dimensional Printing by Shrinking Photonic Crystals. *Nat. Commun.* **2019**, *10* (1), 4340.

(94) Sophonrat, N.; Sandström, L.; Johansson, A.-C.; Yang, W. Co-Pyrolysis of Mixed Plastics and Cellulose: An Interaction Study by Py-GC × GC/MS. *Energy Fuels* **2017**, *31* (10), 11078−11090.

(95) Gissinger, J. R.; Zavada, S. R.; Smith, J. G.; Kemppainen, J.; Gallegos, I.; Odegard, G. M.; Siochi, E. J.; Wise, K. E. Predicting Char Yield of High-Temperature Resins. *Carbon* **2023**, *202*, 336−347.

(96) Pramanick, B.; Vazquez-Pinon, M.; Torres-Castro, A.; Martinez-Chapaa, S. O.; Madou, M. Effect of Pyrolysis Process Parameters on Electrical, Physical, Chemical and Electro-Chemical Properties of SU-8-Derived Carbon Structures Fabricated Using the C-MEMS Process. *Mater. Today Proc.* **2018**, *5* (3), 9669−9682.

(97) Wyss, K. M.; Li, J. T.; Advincula, P. A.; Bets, K. V.; Chen, W.; Eddy, L.; Silva, K. J.; Beckham, J. L.; Chen, J.; Meng, W.; Deng, B.; Nagarajaiah, S.; Yakobson, B. I.; Tour, J. M. Upcycling of Waste Plastic into Hybrid Carbon Nanomaterials. *Adv. Mater.* **2023**, *35* (16), 2209621.

(98) Undri, A.; Frediani, M.; Rosi, L.; Frediani, P. Reverse Polymerization of Waste Polystyrene through Microwave Assisted Pyrolysis. *J. Anal. Appl. Pyrolysis* **2014**, *105*, 35−42.

(99) Natu, R.; Islam, M.; Gilmore, J.; Martinez-Duarte, R. Shrinkage of SU-8 Microstructures during Carbonization. *J. Anal. Appl. Pyrolysis* **2018**, *131*, 17−27.

(100) Martinez-Duarte, R. SU-8 Photolithography as a Toolbox for Carbon MEMS. *Micromachines* **2014**, *5* (3), 766−782.

(101) Sharma, S.; Kamath, R.; Madou, M. Porous Glassy Carbon Formed by Rapid Pyrolysis of Phenol-Formaldehyde Resins and Its Performance as Electrode Material for Electrochemical Double Layer Capacitors. *J. Anal. Appl. Pyrolysis* **2014**, *108*, 12−18.

(102) Hassan, Y. M.; Caviglia, C.; Hemanth, S.; Mackenzie, D. M. A.; Alstrøm, T. S.; Petersen, D. H.; Keller, S. S. High Temperature SU-8 Pyrolysis for Fabrication of Carbon Electrodes. *J. Anal. Appl. Pyrolysis* **2017**, *125*, 91−99.

(103) Sharma, S.; Rostas, A. M.; Bordonali, L.; MacKinnon, N.; Weber, S.; Korvink, J. G. Micro and Nano Patternable Magnetic Carbon. *J. Appl. Phys.* **2016**, *120* (23), 235107.

(104) Sharma, S.; Shyam Kumar, C. N.; Korvink, J. G.; Kübel, C. Evolution of Glassy Carbon Microstructure: In Situ Transmission Electron Microscopy of the Pyrolysis Process. *Sci. Rep.* **2018**, *8* (1), 16282.

(105) Dickens, B. Thermally Degrading Polyethylene Studied by Means of Factor-jump Thermogravimetry. *J. Polym. Sci. Polym. Chem. Ed.* **1982**, *20* (4), 1065−1087.

(106) Rezaei, B.; Hansen, T. W.; Keller, S. S. Stereolithography-Derived Three-Dimensional Pyrolytic Carbon/Mn₃O₄ Nanostructures for Free-Standing Hybrid Supercapacitor Electrodes. *ACS Appl. Nano Mater.* **2022**, *5* (2), 1808−1819.

(107) Cardenas-Benitez, B.; Eschenbaum, C.; Mager, D.; Korvink, J. G.; Madou, M. J.; Lemmer, U.; Leon, I. D.; Martinez-Chapa, S. O. Pyrolysis-Induced Shrinking of Three-Dimensional Structures Fabricated by Two-Photon Polymerization: Experiment and Theoretical Model. *Microsyst. Nanoeng.* **2019**, *5* (1), 38.

(108) Vyatskikh, A.; Kudo, A.; Delalande, S.; Greer, J. R. Additive Manufacturing of Polymer-Derived Titania for One-Step Solar Water Purification. *Mater. Today Commun.* **2018**, *15*, 288−293.

(109) Gomez-Martin, A.; Schnepp, Z.; Ramirez-Rico, J. Structural Evolution in Iron-Catalyzed Graphitization of Hard Carbons. *Chem. Mater.* **2021**, *33* (9), 3087−3097.

(110) Ni, L.; Kuroda, K.; Zhou, L.-P.; Ohta, K.; Matsuishi, K.; Nakamura, J. Decomposition of Metal Carbides as an Elementary Step of Carbon Nanotube Synthesis. *Carbon* **2009**, *47* (13), 3054−3062.

(111) Hoekstra, J.; Beale, A. M.; Soulimani, F.; Versluijs-Helder, M.; Geus, J. W.; Jenneskens, L. W. Base Metal Catalyzed Graphitization of Cellulose: A Combined Raman Spectroscopy, Temperature-Dependent X-Ray Diffraction and High-Resolution Transmission Electron Microscopy Study. *J. Phys. Chem. C* **2015**, *119* (19), 10653−10661.

(112) Bazargan, A.; McKay, G. A Review - Synthesis of Carbon Nanotubes from Plastic Wastes. *Chem. Eng. J.* **2012**, *195−196*, 377−391.

(113) Gong, J.; Liu, J.; Wan, D.; Chen, X.; Wen, X.; Mijowska, E.; Jiang, Z.; Wang, Y.; Tang, T. Catalytic Carbonization of Polypropylene by the Combined Catalysis of Activated Carbon with Ni2O3 into Carbon Nanotubes and Its Mechanism. *Appl. Catal. Gen.* **2012**, *449*, 112−120.

(114) Chen, X.; He, J.; Yan, C.; Tang, H. Novel In Situ Fabrication of Chestnut-Like Carbon Nanotube Spheres from Polypropylene and Nickel Formate. *J. Phys. Chem. B* **2006**, *110* (43), 21684−21689.

(115) Tang, T.; Chen, X.; Meng, X.; Chen, H.; Ding, Y. Synthesis of Multiwalled Carbon Nanotubes by Catalytic Combustion of Polypropylene. *Angew. Chem., Int. Ed.* **2005**, *44* (10), 1517−1520.

(116) Gong, J.; Liu, J.; Wen, X.; Jiang, Z.; Chen, X.; Mijowska, E.; Tang, T. Upcycling Waste Polypropylene into Graphene Flakes on Organically Modified Montmorillonite. *Ind. Eng. Chem. Res.* **2014**, *53* (11), 4173−4181.

(117) Gong, J.; Michalkiewicz, B.; Chen, X.; Mijowska, E.; Liu, J.; Jiang, Z.; Wen, X.; Tang, T. Sustainable Conversion of Mixed Plastics into Porous Carbon Nanosheets with High Performances in Uptake of Carbon Dioxide and Storage of Hydrogen. *ACS Sustain. Chem. Eng.* **2014**, *2* (12), 2837−2844.

(118) Zheng, Y.; Wang, J.; Li, D.; Liu, C.; Lu, Y.; Lin, X.; Zheng, Z. Activity and Selectivity of Ni-Cu Bimetallic Zeolites Catalysts on Biomass Conversion for Bio-Aromatic and Bio-Phenols. *J. Energy Inst.* **2021**, *97*, 58.

(119) Xia, S.; Yang, H.; Lei, S.; Lu, W.; Cai, N.; Xiao, H.; Chen, Y.; Chen, H. Iron Salt Catalytic Pyrolysis of Biomass: Influence of Iron Salt Type. *Energy* **2023**, *262*, 125415.

(120) Zheng, Y.; Wang, J.; Wang, D.; Zheng, Z. Advanced Catalytic Upgrading of Biomass Pyrolysis Vapor to Bio-Aromatics Hydrocarbon: A Review. *Appl. Energy Combust. Sci.* **2022**, *10*, 100061.

(121) Chen, C.; Sun, K.; Wang, A.; Wang, S.; Jiang, J. Catalytic Graphitization of Cellulose Using Nickel as Catalyst. *BioResources* **2018**, *13* (2), 3165−3176.

(122) Hunter, R. D.; Ramírez-Rico, J.; Schnepp, Z. Iron-Catalyzed Graphitization for the Synthesis of Nanostructured Graphitic Carbons. *J. Mater. Chem. A* **2022**, *10* (9), 4489−4516.

(123) Chen, X.; Wang, H.; He, J. Synthesis of Carbon Nanotubes and Nanospheres with Controlled Morphology Using Different Catalyst Precursors. *Nanotechnology* **2008**, *19* (32), 325607.

(124) Nishino, H.; Nishida, R.; Matsui, T.; Kawase, N.; Mochida, I. Growth of Amorphous Carbon Nanotube from Poly-(Tetrafluoroethylene) and Ferrous Chloride. *Carbon* **2003**, *41* (14), 2819−2823.

(125) Inagaki, M.; Park, K. C.; Endo, M. Carbonization under Pressure. *New Carbon Mater.* **2010**, *25* (6), 409−420.

(126) Trick, K. A.; Saliba, T. E. Mechanisms of the Pyrolysis of Phenolic Resin in a Carbon/Phenolic Composite. *Carbon* **1995**, *33* (11), 1509−1515.

(127) Boyce, A. M.; Cumming, D. J.; Huang, C.; Zankowski, S. P.; Grant, P. S.; Brett, D. J. L.; Shearing, P. R. Design of Scalable, Next-Generation Thick Electrodes: Opportunities and Challenges. *ACS Nano* **2021**, *15* (12), 18624−18632.

(128) Fu, X.; Zhou, Y.; Huang, J.; Feng, L.; Yu, P.; Zhang, Q.; Yang, W.; Wang, Y. Rethinking the Electrode Multiscale Microstructures: A Review on Structuring Strategies toward Battery Manufacturing Genome. *Adv. Energy Mater.* **2023**, *13* (32). DOI: 10.1002/aenm.202301385

(129) Bui, J. C.; Lees, E. W.; Pant, L. M.; Zenyuk, I. V.; Bell, A. T.; Weber, A. Z. Continuum Modeling of Porous Electrodes for Electrochemical Synthesis. *Chem. Rev.* **2022**, *122* (12), 11022−11084.

(130) Wu, J.; Ju, Z.; Zhang, X.; Marschilok, A. C.; Takeuchi, K. J.; Wang, H.; Takeuchi, E. S.; Yu, G. Gradient Design for High-Energy and High-Power Batteries. *Adv. Mater.* **2022**, *34* (29), 2202780.

(131) Zhao, Z.; Sun, M.; Chen, W.; Liu, Y.; Zhang, L.; Dongfang, N.; Ruan, Y.; Zhang, J.; Wang, P.; Dong, L.; Xia, Y.; Lu, H. Sandwich, Vertical-Channeled Thick Electrodes with High Rate and Cycle Performance. *Adv. Funct. Mater.* **2019**, *29* (16), 1809196.

(132) Sun, H.; Zhu, J.; Baumann, D.; Peng, L.; Xu, Y.; Shakir, I.; Huang, Y.; Duan, X. Hierarchical 3D Electrodes for Electrochemical Energy Storage. *Nat. Rev. Mater.* **2019**, *4* (1), 45−60.

(133) Mao, J.; Iocozzia, J.; Huang, J.; Meng, K.; Lai, Y.; Lin, Z. Graphene Aerogels for Efficient Energy Storage and Conversion. *Energy Environ. Sci.* **2018**, *11* (4), 772−799.

(134) Yu, Z.-L.; Xin, S.; You, Y.; Yu, L.; Lin, Y.; Xu, D.-W.; Qiao, C.; Huang, Z.-H.; Yang, N.; Yu, S.-H.; Goodenough, J. B. Ion-Catalyzed Synthesis of Microporous Hard Carbon Embedded with Expanded Nanographite for Enhanced Lithium/Sodium Storage. *J. Am. Chem. Soc.* **2016**, *138* (45), 14915−14922.

(135) Xue, X.; Lin, D.; Li, Y. Low Tortuosity 3D-Printed Structures Enhance Reaction Kinetics in Electrochemical Energy Storage and Electrocatalysis. *Small Struct.* **2022**, *3* (12), 2200159.

(136) Khoo, V.; Ng, S.-F.; Haw, C.-Y.; Ong, W.-J. Additive Manufacturing: A Paradigm Shift in Revolutionizing Catalysis with 3D Printed Photocatalysts and Electrocatalysts Toward Environmental Sustainability. *Small* **2024**, *20*, 2401278.

(137) Jorge, A. B.; Jervis, R.; Periasamy, A. P.; Qiao, M.; Feng, J.; Tran, L. N.; Titirici, M.-M. 3D Carbon Materials for Efficient Oxygen and Hydrogen Electrocatalysis. *Adv. Energy Mater.* **2020**, *10* (11), 1902494.

(138) Peng, M.; Shi, D.; Sun, Y.; Cheng, J.; Zhao, B.; Xie, Y.; Zhang, J.; Guo, W.; Jia, Z.; Liang, Z.; Jiang, L. 3D Printed Mechanically Robust Graphene/CNT Electrodes for Highly Efficient Overall Water Splitting. *Adv. Mater.* **2020**, *32* (23), 1908201.

(139) Kou, T.; Wang, S.; Shi, R.; Zhang, T.; Chiovoloni, S.; Lu, J. Q.; Chen, W.; Worsley, M. A.; Wood, B. C.; Baker, S. E.; Duoss, E. B.; Wu, R.; Zhu, C.; Li, Y. Periodic Porous 3D Electrodes Mitigate Gas Bubble Traffic during Alkaline Water Electrolysis at High Current Densities. *Adv. Energy Mater.* **2020**, *10* (46), 2002955.

(140) Wang, H.; Jia, J.; Song, P.; Wang, Q.; Li, D.; Min, S.; Qian, C.; Wang, L.; Li, Y. F.; Ma, C.; Wu, T.; Yuan, J.; Antonietti, M.; Ozin, G. A. Efficient Electrocatalytic Reduction of CO2 by Nitrogen-Doped Nanoporous Carbon/Carbon Nanotube Membranes: A Step Towards the Electrochemical CO2 Refinery. *Angew. Chem., Int. Ed.* **2017**, *56* (27), 7847−7852.

(141) Deshpande, V. S.; Ashby, M. F.; Fleck, N. A. Foam Topology: Bending versus Stretching Dominated Architectures. *Acta Mater.* **2001**, *49* (6), 1035−1040.

(142) Parisien, A.; ElSayed, M. S. A.; Frei, H. Mechanoregulation Modelling of Stretching versus Bending Dominated Periodic Cellular Solids. *Mater. Today Commun.* **2022**, *33*, 104315.

(143) Berger, J. B.; Wadley, H. N. G.; McMeeking, R. M. Mechanical Metamaterials at the Theoretical Limit of Isotropic Elastic Stiffness. *Nature* **2017**, *543* (7646), 533−537.

(144) Natu, R.; Islam, M.; Keck, D.; Martinez-Duarte, R. Automated "Pick and Transfer" of Targeted Cells Using Dielectrophoresis. *Lab. Chip* **2019**, *19* (15), 2512−2525.

(145) Puri, P.; Kumar, V.; Belgamwar, S. U.; Sharma, N. N. Microfluidic Device for Cell Trapping with Carbon Electrodes Using Dielectrophoresis. *Biomed. Microdevices* **2018**, *20* (4), 1−10.

(146) Natu, R.; Islam, M.; Martinez-Duarte, R. Nondimensional Streaming Dielectrophoresis Number for a System of Continuous Particle Separation. *Anal. Chem.* **2019**, *91* (7), 4357−4367.

(147) Elitas, M.; Yildizhan, Y.; Islam, M.; Martinez-Duarte, R.; Ozkazanc, D. Dielectrophoretic Characterization and Separation of Monocytes and Macrophages Using 3D Carbon-Electrodes. *ELECTROPHORESIS* **2019**, *40* (2), 315−321.

(148) Mishra, R.; Pramanick, B.; Maiti, T. K.; Bhattacharyya, T. K. Glassy Carbon Microneedles—New Transdermal Drug Delivery Device Derived from a Scalable C-MEMS Process. *Microsyst. Nanoeng.* **2018**, *4* (1), 1−11.

(149) Devi, M.; Vomero, M.; Fuhrer, E.; Castagnola, E.; Gueli, C.; Nimbalkar, S.; Hirabayashi, M.; Kassegne, S.; Stieglitz, T.; Sharma, S. Carbon-Based Neural Electrodes: Promises and Challenges. *J. Neural Eng.* **2021**, *18* (4), 041007.

(150) Fuhrer, E.; Bäcker, A.; Kraft, S.; Gruhl, F. J.; Kirsch, M.; MacKinnon, N.; Korvink, J. G.; Sharma, S. 3D Carbon Scaffolds for Neural Stem Cell Culture and Magnetic Resonance Imaging. *Adv. Healthc. Mater.* **2018**, *7* (4), 1700915.

(151) Islam, M.; Lantada, A. D.; Gómez, M. R.; Mager, D.; Korvink, J. G. Microarchitectured Carbon Structures as Innovative Tissue-Engineering Scaffolds. *Adv. Eng. Mater.* **2020**, *22* (6), 2000083.

(152) Kronenfeld, J. M.; Rother, L.; Saccone, M. A.; Dulay, M. T.; DeSimone, J. M. Roll-to-Roll, High-Resolution 3D Printing of Shape-Specific Particles. *Nature* **2024**, *627* (8003), 306−312.

(153) Lipkowitz, G.; Samuelsen, T.; Hsiao, K.; Lee, B.; Dulay, M. T.; Coates, I.; Lin, H.; Pan, W.; Toth, G.; Tate, L.; Shaqfeh, E. S. G.; DeSimone, J. M. Injection Continuous Liquid Interface Production of 3D Objects. *Sci. Adv.* **2022**, *8* (39), No. eabq3917.

(154) Coates, I. A.; Pan, W.; Saccone, M. A.; Lipkowitz, G.; Ilyin, D.; Driskill, M. M.; Dulay, M. T.; Frank, C. W.; Shaqfeh, E. S. G.; DeSimone, J. M. High-Resolution Stereolithography: Negative Spaces Enabled by Control of Fluid Mechanics. *Proc. Natl. Acad. Sci. U. S. A.* **2024**, *121* (37), No. e2405382121.

(155) Xia, S.; Li, K.; Xiao, H.; Cai, N.; Dong, Z.; Xu, C.; Chen, Y.; Yang, H.; Tu, X.; Chen, H. Pyrolysis of Chinese Chestnut Shells: Effects of Temperature and Fe Presence on Product Composition. *Bioresour. Technol.* **2019**, *287*, 121444.

(156) Shirolkar, N.; Maffe, A.; DiLoreto, E.; Gulgunje, P.; Gupta, K.; Park, J. G.; Kirmani, M. H.; Liang, R.; Kumar, S. Continuous Small Diameter Carbon Fibers. *Carbon* **2023**, *201*, 1193−1199.

(157) Zhao, Q.; Zhang, K.; Zhu, S.; Xu, H.; Cao, D.; Zhao, L.; Zhang, R.; Yin, W. Review on the Electrical Resistance/Conductivity of Carbon Fiber Reinforced Polymer. *Appl. Sci.* **2019**, *9* (11), 2390.